

Submitted for Publication in the Astrophysical Journal

Chemical Rates on Small Grains and PAHs: C⁺ Recombination and H₂ Formation

Mark G. Wolfire

Department of Astronomy, University of Maryland, College Park, MD 20742-2421

`mwolfire@astro.umd.edu`

A. G. G. M. Tielens

*Space Science and Astrobiology Division, NASA Ames Research Center, MS 245-3, Moffett
Field, CA 94035*

`atielens@mail.arc.nasa.gov`

David Hollenbach

*Space Science and Astrobiology Division, NASA Ames Research Center, MS 245-3, Moffett
Field, CA 94035*

`hollenbach@ism.arc.nasa.gov`

and

M. J. Kaufman

*Department of Physics, San Jose State University, One Washington Square, San Jose, CA
95192-0106*

`mkaufman@email.sjsu.edu`

ABSTRACT

We use observations of the C I, C II, H I, and H₂ column densities along lines of sight in the Galactic plane to determine the formation rate of H₂ on grains and to determine chemical reaction rates with Polycyclic Aromatic Hydrocarbons. Photodissociation region models are used to find the best fit parameters to the observed columns. We find the H₂ formation rate on grains has a low rate ($R \sim$

$1 \times 10^{-17} \text{ cm}^3 \text{ s}^{-1}$) along lines of sight with low column density ($A_V \lesssim 0.25$) and low molecular fraction ($f_{\text{H}_2} \lesssim 10^{-4}$). At higher column densities ($0.25 \leq A_V \leq 2.13$), we find a rate of $R \sim 3.5 \times 10^{-17} \text{ cm}^3 \text{ s}^{-1}$. The lower rate at low column densities could be the result of grain processing by interstellar shocks which may deplete the grain surface area or process the sites of H + H formation, thereby inhibiting H₂ production. Alternatively, the formation rate may be normal, and the low molecular fraction may be the result of lines of sight which graze larger clouds. Such lines of sight would have a reduced H₂ self-shielding compared to the line-of-sight column. We find the reaction $\text{C}^+ + \text{PAH}^- \rightarrow \text{C} + \text{PAH}^0$ is best fit with a rate $2.4 \times 10^{-7} \Phi_{\text{PAH}} T_2^{-0.5} \text{ cm}^3 \text{ s}^{-1}$ with $T_2 = T/100 \text{ K}$ and the reaction $\text{C}^+ + \text{PAH}^0 \rightarrow \text{C} + \text{PAH}^+$ is best fit with a rate $8.8 \times 10^{-9} \Phi_{\text{PAH}} \text{ cm}^3 \text{ s}^{-1}$. In high column density gas we find $\Phi_{\text{PAH}} \sim 0.4$. In low column density gas, Φ_{PAH} is less well constrained with $\Phi_{\text{PAH}} \sim 0.2 - 0.4$.

Subject headings: astrochemistry–ISM: clouds–ISM: general—ISM: molecules

1. INTRODUCTION

Much of the chemistry in the interstellar medium (ISM) proceeds via two body gas phase reactions; however, based on reaction time arguments it is well established that the formation of H₂ must proceed predominantly by grain surface reactions (Hollenbach & Salpeter 1971) and thus the equilibrium abundance of H₂ in diffuse gas depends on the balance between dissociation from ultraviolet radiation and the formation on grains. In addition, Lepp et al. (1988) suggested that in diffuse clouds, reactions with small grains or large molecules can affect the charge balance and abundance of metal ions. More recent theoretical (e.g., Bakes & Tielens 1998; Weingartner & Draine 2001; Wolfire et al. 2003; Lipshtat & Biham 2003; Chang et al. 2006) and laboratory, (Cazaux & Tielens 2004) investigations have explored the rates of H₂ formation and chemical reactions on surfaces of small grains and their dependence on environmental factors. The chemical rates have been difficult to pin down in part because the exact abundance, type, surface area, and physical properties of the grains/large molecules are not well determined.

Studies with a more observational approach have also estimated H₂ formation rates and chemical rates with grains (e.g., Jura 1975; Browning et al. 2003; Welty et al. 2003). Jura (1975) estimated a formation rate of about $R \sim 3 \times 10^{-17} \text{ cm}^3 \text{ s}^{-1}$ in diffuse gas of low column density; however, one could see in the *Copernicus* survey of Savage et al. (1977) that a single H₂ formation rate can not explain all of the observed column densities even accounting for the expected variation in ultraviolet radiation field and gas density. A more recent analysis

by Gry et al. (2002) using data from the *Far Ultraviolet Spectroscopic Explorer* (FUSE) find a formation rate of $R \sim 4 \times 10^{-17} \text{ cm}^3 \text{ s}^{-1}$ in diffuse gas and Browning et al. (2003) estimates the rate at 2.5 - 10 times lower in the low metallicity environments of the Large and Small Magellanic Clouds. Habart et al. (2004) suggests that the H_2 formation rate varies in molecular clouds exposed to intense radiation by a factor of about five, perhaps due to the temperature dependence of the formation process on grain surfaces (Cazaux & Tielens 2004). In this paper we take a semi-empirical approach by allowing the ensemble of recent observations to guide us in the proper “astrophysical” rates rather than use rates based on laboratory measurements with an assumed grain type and distribution.

Bakes & Tielens (1998) investigated the effects of Polycyclic Aromatic Hydrocarbons (PAHs) on the chemistry of dense regions exposed to intense ultraviolet radiation. They found that charge exchange reactions with PAHs are important in setting the column density of neutral metals, in particular C I. Welty et al. (2003) found patterns of neutral column densities in diffuse clouds higher than suggested by electron recombination alone and suggested that recombination on grains might be important. Weingartner & Draine (2001) carried out a detailed analysis of the “grain assisted” rates required to explain the observed column densities along the line of sight to 23 Ori. Wolfire et al. (1995, 2003) found that reactions with PAHs can affect the ionization balance of metals and also atomic hydrogen, in diffuse gas, in particular in the warm neutral medium. This has an important effect on the grain charge and thus the heating produced by the grain photoelectric effect; the dominant heating process in the diffuse ISM.

In Wolfire et al. (2003) we adopted rates with PAHs based on the Draine & Sutin (1987) formalism for interactions with small grains, but modified the rates to match a preliminary assessment of the observed $N_{\text{C I}}/N_{\text{C II}}$ ratio in diffuse gas. This ratio is a particularly good diagnostic because carbon is abundant, the rates of C^+ recombination on PAH anions effectively compete with electron recombination, and carbon exists in the diffuse ISM outside of H II regions as either C I or C II but not higher ionization stages.

For several years, the *Copernicus* column densities of H I (Bohlin et al. 1978), H_2 (Savage et al. 1977), C I (Jenkins & Shaya 1979; Jenkins et al. 1983), and C II (Hobbs et al. 1982) were the only data available. More recently the combined observations from the *Hubble Space Telescope* Goddard High Resolution Spectrograph (GHRS) and Space Telescope Imaging Spectrograph (STIS) instruments along with the *Far Ultraviolet Spectroscopic Explorer* (FUSE) have produced many more sight lines to study in particular in H_2 (e.g., Rachford et al. 2002; Cartledge et al. 2004), C I (e.g., Zsargo et al. 1997; Zsargó & Federman 2003), and C II (e.g., Sofia et al. 2004). In § 2 we present the observations used in this study and in § 3 we discuss our cloud models and our fitting procedure. In § 4 we present our

results for the best fit rates for grain reactions and for H_2 formation. We also discuss some of the interesting sight lines which seem to have outlying points. We summarize our main conclusions in § 5.

2. OBSERVATIONS

Observations of the H I, H_2 , C I, and C II columns are listed in Table 1 and are taken from the literature as noted. We have included only those lines of sight which have measured values of $\log N_{\text{HI}}$, $\log N_{\text{H}_2}$, and $\log N_{\text{CI}}$, and have not included lines of sight with upper or lower limits in these quantities. The C II column is measured directly only towards thirteen sources (Sofia et al. 2004). Six of these have definite C I columns and are included in our sample. For all other sources we use the conversion $N_{\text{CII}} = \mathcal{A}_{\text{C}} \times N$ where $N \equiv N_{\text{HI}} + 2N_{\text{H}_2}$, and $\mathcal{A}_{\text{C}} = 1.6 \times 10^{-4}$ is the mean gas phase abundance of carbon per hydrogen nucleus found by Sofia et al. (2004) from all measured values of the C II carbon abundance in the diffuse ISM.

Most of the H I and H_2 columns and uncertainties are from the *Copernicus* ultraviolet absorption spectroscopy observations of Bohlin et al. (1978) and Savage et al. (1977). More recently, Cartledge et al. (2004) updated several of these lines of sight with FUSE observations. The columns are in good agreement with the previous results, but with smaller quoted uncertainties. In cases of overlap we use the Cartledge et al. (2004) results. Additional H_2 columns are provided by FUSE surveys (e.g., Rachford et al. 2002). In several low column density lines of sight Savage et al. (1977) did not quote an uncertainty for the H_2 columns. In these cases we use the uncertainty $\sigma(\log N_{\text{H}_2}) = 0.20$ as suggested by D. Welty¹ and is comparable to the maximum quoted value for all observations.

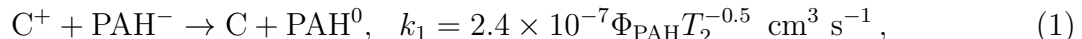
Many of the N_{CI} columns are from the *Copernicus* ultraviolet absorption observations of Jenkins & Shaya (1979) and Jenkins et al. (1983). Additional C I columns are provided for example, by GHRS observations and FUSE (Zsargo et al. 1997; Zsargó & Federman 2003; Jenkins & Tripp 2001). The method used by Jenkins & Tripp (2001) to determine C I columns does not yield a direct measure of the random errors in the observed velocity integrated column density. We adopt an uncertainty comparable to similar STIS and *FUSE* observations at similar column densities (e.g., Sonnentrucker et al. 2002).

¹<http://astro.uchicago.edu/home/web/welty/coldens.html>

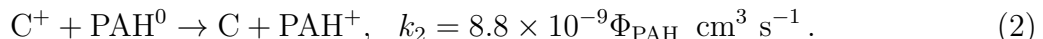
3. MODELS

3.1. Reaction Rates with PAHs and Carbon Chemistry

The PAH rates in Wolfire et al. (2003) were calculated using the equations given by Draine & Sutin (1987) for a disk shaped PAH with the number of Carbon atoms $N_C = 35$ and a PAH abundance of 6×10^{-7} per hydrogen nucleus. Wolfire et al. (2003) found it necessary to modify the rates by a factor Φ_{PAH} to match a preliminary assessment of the observed $N_{\text{CI}}/N_{\text{CII}}$ ratio in the diffuse ISM. The factor Φ_{PAH} is to include a wide range of unknowns in the rates including the PAH size, geometry, and abundance. Although the full Draine & Sutin (1987) formalism is used in our code, over typical temperatures and densities found in the diffuse ISM the rates can be closely approximated by simple formulae. For C^+ recombination on PAHs we have

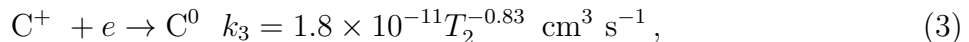


where $T_2 \equiv T/(100 \text{ K})$, and for charge exchange



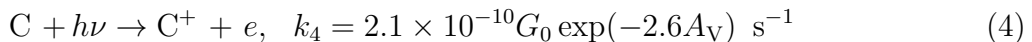
Several rates were given in Wolfire et al. (2003) Appendix C2, mainly related to the charge balance for hydrogen and the electron abundance. We provide a summary of our rate set in Appendix A.

In addition to reactions with PAHs, C^+ can also recombine with electrons in the gas phase via radiative or dielectronic recombination. It has recently come to our attention that dielectronic recombination of C^+ can be significant in diffuse gas (G. Ferland, private communication). The total (dielectronic plus radiative) rates by Altun et al. (2004) and those posted on-line for lower temperatures by Badnell (<http://amdpp.phys.strath.ac.uk/tamoc/DATA/>) are higher by a factor of ~ 2 at 100 K than rates by Nahar & Pradhan (1997). For the majority of this paper we use the Badnell rates, but discuss the implications if they are lower as suggested by the previous data. A fit to the total rate is given by



where the fit is good to within 8% for $20 \text{ K} < T < 300 \text{ K}$.

The C^+ is formed mainly by the photoionization of C by the interstellar radiation field



where G_0 is the FUV ($6 \text{ eV} \leq h\nu \leq 13.6 \text{ eV}$) interstellar radiation field measured in units of the Habing (1968) field ($G_0 = 1$ is $1.3 \times 10^{-4} \text{ erg cm}^{-2} \text{ s}^{-1} \text{ sr}^{-1}$). In Wolfire et al.

(2003), we adopted $G_0 = 1.7$, a field strength comparable to the Draine (1978) interstellar field. Balancing formation and destruction processes, in clouds optically thin to the FUV radiation, the $N_{\text{CI}}/N_{\text{CII}}$ ratio is mainly a function of $n\Phi_{\text{PAH}}/G_0$.

3.2. H₂ Formation

Molecular hydrogen formation in diffuse gas proceeds via reactions with atomic hydrogen on grain surfaces. We adopt a formation rate per unit volume which goes as $nn_{\text{HI}}R$ where n is the hydrogen nucleus density, n_{HI} is the density of atomic hydrogen, and R is a constant of order $3 \times 10^{-17} \text{ cm}^3 \text{ s}^{-1}$. The constant includes the surface area of grains per hydrogen nucleus. (If the metallicity were to vary as Z , and the grain surface area per H proportional to Z , then the rate R would go as Z .) Previous investigators have included both a gas and grain temperature dependence in this rate equation intended to include the collision rate of atomic hydrogen with grains, the sticking coefficient of hydrogen on grains (which is a function of both the hydrogen temperature and grain temperature), and the thermal diffusion of atoms across grain surfaces and thermal evaporation from these surfaces (which is a function of the grain temperature). The collision rate increases with temperature while the sticking coefficient and formation efficiency decrease with temperature (Hollenbach & Salpeter 1971; Burke & Hollenbach 1983; Pirronello et al. 1999; Cazaux & Tielens 2004). In light of the uncertainties of the details of the various processes, Kaufman et al. (1999) adopted an average rate which was independent of temperature.

The dissociation rate of H₂ per unit volume goes as

$$G_0 I n_{\text{H}_2} \beta(N_{\text{H}_2}) \exp(-2.5A_V) \quad (5)$$

where I is the unshielded photodissociation rate in the local interstellar field ($G_0 = 1$), and $\beta(N_{\text{H}_2})$ is the H₂ self-shielding factor. We take $I = 4.7 \times 10^{-11} \text{ s}^{-1}$ from Abgrall et al. (1992). The unshielded rate could change depending on the detailed population of the molecular hydrogen rotational and vibrational levels resulting from different incident FUV fields, gas densities, and temperatures. We have compared our constant unshielded dissociation rate I , with results produced with the code available on-line from the Meudon Group². As discussed in Le Petit et al. (2006) they include a more detailed treatment of H₂ dissociation and shielding. We ran their code at $n = 30$ and 100 cm^{-3} , $G_0 = 1.7$, and $A_V = 0.1, 0.3$, and 1 , and found good agreement with less than a 10% difference in values of I . We use the self-shielding factor from Draine & Bertoldi (1996) (their equation 37) which is a fit to

²See <http://aristote.obspm.fr/MIS>

their detailed H₂ destruction calculation. The equilibrium molecular fraction $2n_{\text{H}_2}/(n_{\text{HI}} + 2n_{\text{H}_2})$, for unshielded H₂ ($\beta = 1$) equals $2nR/G_0I$. For constant I , the molecular fraction is proportional to $2nR/G_0$. Thus, to first order and ignoring shielding by dust or H₂, the $N_{\text{C I}}/N_{\text{C II}}$ ratio depends on $\Phi_{\text{PAH}}n/G_0$ while the $N_{\text{H}_2}/N_{\text{HI}}$ ratio depends on Rn/G_0 .

3.3. 2-Sided Models

We see from sections 3.1 and 3.2 that the $N_{\text{C I}}/N_{\text{C II}}$ ratio and the H₂ column N_{H_2} depends on Φ_{PAH} , R , and the ratio of G_0/n . The total column density $N = N_{\text{HI}} + 2N_{\text{H}_2}$ also enters due to the extinction of the incident FUV field in equations (4) and (5) and also in the self-shielding factor β (which depends on the H₂ column density). The total column density is known for each source. Thus we can construct models for each source by holding the total column density fixed, and varying G_0/n , Φ_{PAH} , and R , until good fits are obtained to the observed column densities, $N_{\text{C I}}/N_{\text{C II}}$ and $2N_{\text{H}_2}/N$.

Since many of the observations have cloud columns $A_V \lesssim 1$ the effects of radiation incident on the near and far side of the cloud need to be included. This radiation affects both the photoionization of C and the dissociation of H₂. We have modified the 1-sided Photodissociation Region (PDR) code of Kaufman et al. (1999) to include the 2-sided incident radiation. The code calculates the equilibrium chemical abundances and gas temperature in a gas layer exposed to X-rays and FUV radiation. In the one-sided case, calculation of the chemistry, cooling, and line transfer proceeds from the surface to the cloud center in a single pass since these parameters depend only on the cloud properties closer to the surface. In the two-sided case, at a given point in the cloud, the optical depth in the cooling lines and the H₂ column is required towards both surfaces, thus an iterative procedure is required. We first calculate the structure of a cloud illuminated from one side to a depth of one-half the visual extinction of the desired two-sided model. This provides us with initial estimates of line optical depths as well as shielding columns of H₂ and CO. We then iterate the chemical abundance profiles, optical depths, and shielding factors.

We have further modified the physics and chemistry of the Kaufman et al. (1999) code according to the discussion in Wolfire et al. (2003) who assumed a higher abundance of PAHs and a slower rate of interaction of ions and PAHs. These changes largely offset each other, with a resulting minor effect on the grain heating rates and ion chemistry. In addition, we have adopted the results of Péquignot (1990) for the rate coefficient for collisional excitation of O I by H, and those of McCall et al. (2003) for the H₃⁺ dissociative recombination rate coefficient. We have also included the illumination of the cloud by the interstellar soft X-ray radiation field as discussed in Wolfire et al. (2003). Results from this 2-sided code have been

previously presented in Neufeld et al. (2005), and Snow & McCall (2006).

We have compared our calculated H₂ column densities with those produced by the Meudon code. For the same model parameters in section 3.2, and running the code in 2-sided mode, we find that our H₂ columns agree to within a factor of 2 (with our columns lower) and with the largest difference at low column densities ($A_V \sim 0.1$). The agreement is within the typical observational error.

3.4. Fitting Φ_{PAH} and R

We determine the best fit Φ_{PAH} and R by computing a grid of models consisting of 12 values of Φ_{PAH} (0.01, 0.1, 0.2, 0.3, 0.4, 0.5, 0.6, 0.7, 0.8, 0.9, 1.0, 1.1) and 11 values of R (0.5, 1, 2, 3, 4, 5, 6, 7, 8, 9, 10) $\times 10^{-17}$ cm³ s⁻¹. At each grid point, (i.e., for fixed Φ_{PAH} and R), we find the best fit G_0/n values for each source by minimizing the χ_s^2

$$\chi_s^2(\Phi_{\text{PAH}}, R) = \left\{ \frac{\log f_{\text{H}_2}^{\text{model}} - \log f_{\text{H}_2}}{\sigma[\log f_{\text{H}_2}]} \right\}^2 + \left\{ \frac{\log f_{\text{C I}}^{\text{model}} - \log f_{\text{C I}}}{\sigma[\log f_{\text{C I}}]} \right\}^2, \quad (6)$$

where χ_s^2 is the χ^2 value for source s , f_{H_2} and $f_{\text{C I}}$ are the observed values for the column density ratios $f_{\text{H}_2} = 2N_{\text{H}_2}/[N_{\text{H I}} + 2N_{\text{H}_2}]$, $f_{\text{C I}} = N_{\text{C I}}/N_{\text{C II}}$, $f_{\text{H}_2}^{\text{model}}$, and $f_{\text{C I}}^{\text{model}}$ are the calculated values of f_{H_2} and $f_{\text{C I}}$ (dependent upon N – which is measured, and on the unknowns Φ_{PAH} , R , and G_0/n).

We will calculate the χ^2 value over a subset of the sources within a range of A_V values. Thus the reduced χ^2 value at grid point (Φ_{PAH}, R) is the sum over sources within the restricted A_V bin:

$$\chi^2(\Phi_{\text{PAH}}, R) = \sum_s^{N_s} \chi_s^2 / (N_s - 2). \quad (7)$$

where N_s is the total number of sources in the bin.

We find the uncertainty in the measurements $\sigma(\log f_{\text{H}_2})$ and $\sigma(\log f_{\text{C I}})$ using the quoted uncertainties $\sigma(\log N_{\text{H I}})$, $\sigma(\log N_{\text{H}_2})$, $\sigma(\log N_{\text{C I}})$, for the H I, H₂, and C I columns, along with the standard propagation of error formula (e.g., Taylor 1997). Thus

$$\sigma(\log f_{\text{H}_2}) = [\sigma(\log N_{\text{H}_2})^2 + \sigma(\log N)^2]^{1/2}, \quad (8)$$

where $\sigma(\log N)$ is the uncertainty in the total column density,

$$\sigma(\log N) = [\sigma(\log N_{\text{H}_2})^2 f_{\text{H}_2}^2 + \sigma(\log N_{\text{H I}})^2 f_{\text{H I}}^2]^{1/2}, \quad (9)$$

and f_{HI} is the fraction of atomic hydrogen $f_{\text{HI}} = N_{\text{HI}}/[N_{\text{HI}} + 2N_{\text{H}_2}]$. For observed C II column densities, the uncertainty in $\log f_{\text{CI}}$ is given by

$$\sigma(\log f_{\text{CI}}) = [\sigma(\log N_{\text{CI}})^2 + \sigma(\log N_{\text{CII}})^2]^{1/2}, \quad (10)$$

while for estimated C II column densities the uncertainty in $\log f_{\text{CI}}$ is given by

$$\sigma(\log f_{\text{CI}}) = [\sigma(\log N_{\text{CI}})^2 + \sigma(\log N)^2]^{1/2}. \quad (11)$$

In practice, for the χ^2 test, we set $G_0 = 1.7$ and vary n . We estimate the initial range of n values from the analytic expressions in Appendix B. We run models stepping in values of n until we cross the minimum in χ^2 . Then we apply a parabolic interpolation to find the minimum χ^2 and associated values of density and column densities.

4. RESULTS and DISCUSSION

4.1. Fixed Column Density Models

We first carry out model runs for four fixed cloud column densities $A_V = 0.1, 0.5, 1.0,$ and 1.5 with variable $\Phi_{\text{PAH}}, R,$ and G_0/n . The data and model results are displayed in plots of $N_{\text{CI}}/N_{\text{CII}}$ versus f_{H_2} with source column densities grouped in four A_V bins. These plots are intended to show the range of observed values, the effects of varying Φ_{PAH} and R , and an “eye ball” assessment of reasonable values. The A_V bins span the range of observed A_V values with the smallest being $A_V = 0.03$ and the largest $A_V = 2.13$. The A_V bins have been chosen to display natural groupings of the data which we further test using the χ^2 results.

We present in Figure 1 the observed and calculated ratio of $N_{\text{CI}}/N_{\text{CII}}$ versus f_{H_2} for observations in the range $0.03 \lesssim A_V \lesssim 0.25$ and $N_{\text{H}_2} \lesssim 10^{17} \text{ cm}^{-2}$. Figure 1 focuses on the low f_{H_2} ($\lesssim 10^{-4}$) and low A_V directions. The curves are for a model cloud column density of $A_V = 0.1$, with $G_0 = 1.7$ and 5.1 , and density points at $n = 10, 20, 30,$ and 40 cm^{-3} (with the exception of two curves with three density points at $n = 5, 10,$ and 20 cm^{-3}). Diamonds (\diamond) indicate models with $G_0 = 1.7$ and triangles (\triangle) indicate models with $G_0 = 5.1$. We have labeled the model curves with their corresponding values of $\Phi_{\text{PAH}}/R_{-17}$ where $R_{-17} = R/1 \times 10^{-17}$. The curves with $\Phi_{\text{PAH}}/R_{-17} \leq 1/3$ use $R = 3 \times 10^{-17} \text{ cm}^3 \text{ s}^{-1}$ with values of $\Phi_{\text{PAH}} = 1$ ($\Phi_{\text{PAH}}/R_{-17} = 1/3$), $\Phi_{\text{PAH}} = 0.5$ ($\Phi_{\text{PAH}}/R_{-17} = 1/6$), and $\Phi_{\text{PAH}} = 0.01$ ($\Phi_{\text{PAH}}/R_{-17} = 1/300$). We have added three additional curves with lower values of R namely $R = 2 \times 10^{-17} \text{ cm}^3 \text{ s}^{-1}$, $\Phi_{\text{PAH}} = 1$ ($\Phi_{\text{PAH}}/R_{-17} = 1/2$); $R = 1 \times 10^{-17} \text{ cm}^3 \text{ s}^{-1}$, $\Phi_{\text{PAH}} = 0.5$ ($\Phi_{\text{PAH}}/R_{-17} = 1/2$); and $R = 1 \times 10^{-17} \text{ cm}^3 \text{ s}^{-1}$, $\Phi_{\text{PAH}} = 1.0$ ($\Phi_{\text{PAH}}/R_{-17} = 1$) and one

additional curve with higher values of Φ_{PAH} namely $R = 2 \times 10^{-17} \text{ cm}^3 \text{ s}^{-1}$, $\Phi_{\text{PAH}} = 2.0$ ($\Phi_{\text{PAH}}/R_{-17} = 1$).

The curves with the same value of $\Phi_{\text{PAH}}/R_{-17}$, although not exactly the same, differ by less than a factor of 1.5. We see that values of the ratio $\Phi_{\text{PAH}}/R_{-17} \approx 1/2 - 1/3$ are required to match the bulk of the observations. For $\Phi_{\text{PAH}} \leq 1$ this requires $R \leq 2 \times 10^{-17} \text{ cm}^3 \text{ s}^{-1}$ and an H_2 formation rate smaller than the standard $3 \times 10^{-17} \text{ cm}^3 \text{ s}^{-1}$ is necessary.

The subsequent Figures (2, 3, and 4) focus on the high molecular abundance lines of sight ($f_{\text{H}_2} > 10^{-3}$ and $N_{\text{H}_2} > 10^{18} \text{ cm}^{-2}$). The observations are limited to the range $0.25 \lesssim A_V \lesssim 0.75$ (Fig. [2]), $0.75 \lesssim A_V \lesssim 1.25$ (Fig. [3]), and $1.25 \lesssim A_V \lesssim 2.13$ (Fig. [4]) and model curves are for $A_V = 0.5$ (Fig. [2]), $A_V = 1.0$ (Fig. [3]), and $A_V = 1.5$ (Fig. [4]). The models all use $R = 3 \times 10^{-17} \text{ cm}^3 \text{ s}^{-1}$ with values of $\Phi_{\text{PAH}} = 0.01, 0.5, \text{ and } 1.0$, and density, $n = 10, 30, 100, \text{ and } 300 \text{ cm}^{-3}$. Comparing Figures 1 and 2 we see a large jump in the molecular fraction with no observations at intermediate values. This jump is probably the result of the abrupt turn on of molecular hydrogen due to the effects of self-shielding. Self-shielding of H_2 at $N \geq 5 \times 10^{20} \text{ cm}^{-2}$ ($A_V \geq 0.25$) was seen in the Savage et al. (1977) data and also in the more recent FUSE surveys (Gillmon & Shull 2006). In Figure 2, two obvious outliers are 23 Ori ($A_V = 0.28$) at high $N_{\text{C I}}/N_{\text{C II}}$ ratio ($= 1.1 \times 10^{-2}$) and π Sco ($A_V = 0.28$) at low $N_{\text{C I}}/N_{\text{C II}}$ ratio ($= 1.2 \times 10^{-3}$). These are excluded from the χ^2 tests and discussed further in subsection 4.5.

The variation of the curves shown in Figures 1 through 4 as functions of G_0/n , ϕ_{PAH} , and R is discussed in Appendix B. Points with the same $G_0/(nR)$ and fixed column, or A_V , have the same molecular fraction f_{H_2} independent of Φ_{PAH} . At the highest values of G_0/n the molecular fraction is lowest due to rapid photodissociation of molecular hydrogen. In the limit of no H_2 self-shielding and no dust extinction, the limiting molecular fraction is given by $f_{\text{H}_2} = 2nR/(G_0I)$. As G_0/n decreases, the molecular fraction increases with a limiting value of $f_{\text{H}_2} = 1$ for fully molecular gas. As the cloud column density (and thus A_V) increases the local FUV field drops due to dust extinction and the molecular fraction rises due to a lower H_2 photodissociation rate. In addition, the self-shielding by H_2 raises the molecular fraction as the column density increases.

The variation in the $N_{\text{C I}}/N_{\text{C II}}$ ratio can be understood in four limiting regimes: high/low Φ_{PAH} , and high/low G_0/n . First consider the high Φ_{PAH} (0.5 and 1.0) curves. For low G_0/n the destruction of C^+ is dominated by recombination on PAH^- and $N_{\text{C I}}/N_{\text{C II}} \propto \Phi_{\text{PAH}}^2(n/G_0)^2$ (See Appendix C, eq. [C1]). For high G_0/n , the destruction of C^+ is dominated by charge exchange with PAH^0 and electron recombination and thus $N_{\text{C I}}/N_{\text{C II}} \propto \Phi_{\text{PAH}}n/G_0$ (eq. [C2]). In the case of low $\Phi_{\text{PAH}} = 0.01$ the C^+ destruction is dominated by recombination with free electrons n_e . For low G_0/n the electrons are provided by photoionization of C, and

$N_{\text{CI}}/N_{\text{CII}} \propto n/G_0$ (eq. [C3]). For high G_0/n , i.e., low values of n , the electrons are provided by the soft-X ray ionization of H, and $N_{\text{CI}}/N_{\text{CII}} \propto n^{1/2}/G_0$ (eq. [C4]). In the molecular hydrogen case, the molecular fraction increases with column density due to the drop in FUV field and larger H_2 self-shielding. However, in the case of the $N_{\text{CI}}/N_{\text{CII}}$ ratio, it is just the dust extinction that leads to the increase in the ratio with column.

4.2. χ^2 Results

We next present the χ^2 results obtained by binning the sources in four A_V bins. But note that for each source model, we fix A_V to the observed column. Figure 5 shows the results for sources in the range $0.03 \lesssim A_V \lesssim 0.25$ and $N_{\text{H}_2} < 10^{17} \text{ cm}^{-2}$. There appears to be two local minima: one at low R values with $R = 1 \times 10^{-17} \text{ cm}^3 \text{ s}^{-1}$ and $0.2 \lesssim \Phi_{\text{PAH}} \lesssim 0.4$ and one at $R \approx 2 \times 10^{-17} \text{ cm}^3 \text{ s}^{-1}$ and $\Phi_{\text{PAH}} \gtrsim 1$. The $N_{\text{CI}}/N_{\text{CII}}$ ratios in this A_V range are $\lesssim 10^{-3}$ and both equations (B15) and (B17) apply. At low Φ_{PAH} the C^+ destruction by electron recombinations dominate (right hand side of eq. B17) and the dependence on Φ_{PAH} drops out. Moving to the upper right in the χ^2 plot corresponds to lower densities and higher temperatures. There, electron recombination is less effective in producing C I, the C I abundance drops, and the fits become poorer. At sufficiently high Φ_{PAH} , the PAH reactions dominate, the C I abundance rises, and the fits improve. We shall demonstrate that the low R and Φ_{PAH} minimum corresponds to gas densities that are closer to those expected for the diffuse ISM and are therefore favored. The minimum $\chi_{\text{min}}^2 = 1.6$ and lies within a closed set of contours.

We next show the results for sources in the remaining A_V ranges $0.25 \lesssim A_V \lesssim 0.75$ (Fig. [6]: 10 sources), $0.75 \lesssim A_V \lesssim 1.25$ (Fig. [7]: 12 sources), and $0.25 \lesssim A_V \lesssim 2.13$ (Fig. [8]: 28 sources). In these χ^2 plots we do not consider the exact position of the minimum to be as significant as in Figure 5 since it generally lies in a trough of low values within open contours. An approximate fit to the minimum trough is given by

$$\Phi_{\text{PAH}} = 0.22 \left(\frac{R}{10^{-17} \text{ cm}^3 \text{ s}^{-1}} \right) - 0.40 \quad R \gtrsim 3 \times 10^{-17} \text{ cm}^3 \text{ s}^{-1} \quad . \quad (12)$$

and shown in Figure 8.

The χ^2 contours shows that R and Φ_{PAH} are correlated. The minimum lies at roughly a 45 degree angle with Φ_{PAH} proportional to R . For a given observation, that is a fixed f_{H_2} , and A_V , from equation (B9), the ratio Rn/G_0 must be constant along the line of minimum χ^2 . In addition, for a fixed $N_{\text{CI}}/N_{\text{CII}}$, from equations (B15) and (B17) the ratio $G_0/(n\Phi_{\text{PAH}})$ must be constant along the line of minimum χ^2 . Together these imply that R/Φ_{PAH} must be constant or $R \propto \Phi_{\text{PAH}}$.

There is a suggestion from our figures that the best fit Φ_{PAH} and R increases with column density. For $0.25 \lesssim A_V \lesssim 0.75$ (Fig. [6]) the minimum χ^2 lies at $R = 3 \times 10^{-17} \text{ cm}^3 \text{ s}^{-1}$, and $\Phi_{\text{PAH}} = 0.2$, while for $0.75 \lesssim A_V \lesssim 1.25$ (Fig. [7]), there is a minimum trough that extends from $R = 4 \times 10^{-17} \text{ cm}^3 \text{ s}^{-1}$, and $\Phi_{\text{PAH}} = 0.4$ to $R = 6 \times 10^{-17} \text{ cm}^3 \text{ s}^{-1}$, and $\Phi_{\text{PAH}} = 1.0$. If this effect is real then it is not entirely clear what is the physical reason behind it. Perhaps shock processing along low A_V lines of sight tend to reduce grain surface area and produce smaller R (and therefore smaller Φ_{PAH} since $\Phi_{\text{PAH}} \propto R$). The statistics however, are rather poor for separate A_V bins and additional observations are required to confirm the trend.

Note that as the H_2 formation rate R increases the density n must decrease (for fixed G_0) in order to maintain the same molecular fraction. At some large value of R the densities become much lower than typically observed in the diffuse ISM. In Figures 5 and 8 each R and Φ_{PAH} grid point has several sources contributing to the χ^2 value and there is a best fit density for each source. We show in Figures 9 and 10 the average density $\langle n \rangle$, obtained by averaging the best fit density over the sources contributing to each R and Φ_{PAH} grid point. Recall that in computing the χ^2 grid we are finding the best fit ratio G_0/n and have fixed G_0 at 1.7. Thus the density could be higher for higher G_0 . Also shown in Figure 10 is the line along the χ^2 minimum trough (eq.[12]). The density plot (Fig. 10) combined with the χ^2 plot (Fig. 8) shows that the typical diffuse cloud ($n \sim 30 \text{ cm}^{-3}$, $G_0 \sim 1.7$) lies at $R \approx 3.5 \times 10^{-17} \text{ cm}^3 \text{ s}^{-1}$ and $\Phi_{\text{PAH}} = 0.4$. For the low column densities, the contours centered on $R \approx 1 \times 10^{-17} \text{ cm}^3 \text{ s}^{-1}$, and $\Phi_{\text{PAH}} = 0.2 - 0.4$ correspond to gas densities closer to that expected in diffuse gas and we therefore favor these over the larger R and Φ_{PAH} values.

4.3. Effects of C^+ Recombination Rate

The recombination rate of C^+ with electrons is most important at low ϕ_{PAH} or high values of G_0/n (see Appendix B). The total rates (including dielectronic recombination) of Nahar & Pradhan (1997) are higher by a factor of ~ 2 at 100 K compared to Altun et al. (2004) and further diverge at lower temperatures. The $N_{\text{CI}}/N_{\text{CII}}$ ratio can thus vary by a factor of ~ 2 when C^+ recombination with electrons dominates the production of C I. In previous sections of this paper we have used the higher rates, but since the rates are uncertain, we have also investigated the effects of the lower rates. Figure 11 shows the resulting χ^2 plot for the range of column densities $0.25 \lesssim A_V \lesssim 2.13$ and $N_{\text{H}_2} > 10^{18} \text{ cm}^{-2}$. The effects of the Nahar & Pradhan (1997) rates more narrowly constrain the best values of ϕ_{PAH} and R by excluding the parameter space of low ϕ_{PAH} and large R . This is because of the decreased importance of the electron recombination rates and thus the observed $N_{\text{CI}}/N_{\text{CII}}$ ratio can only be achieved through higher PAH reaction rates. The best fit minimum trough,

however, is not changed significantly compared to Figure 8, with only a slight extension to lower $R \sim 2.0 \times 10^{-17} \text{ cm}^3 \text{ s}^{-1}$ and $\phi_{\text{PAH}} \sim 0.2$.

4.4. $A_V < 0.25$ Lines of Sight

For our low column density lines of sight, the combination of a low molecular hydrogen fraction, f_{H_2} and a relatively high $N_{\text{CI}}/N_{\text{CII}}$ ratio indicate that R must be low or at least a low ratio of R/Φ_{PAH} (ref. Figs. [1] and [5]). Are there unusual physical conditions, or additional destruction processes that are acting in these regions which could account for the low H_2 columns? We first consider the effects of warm neutral medium (WNM) along the line of sight. The WNM consists of low density ($n \sim 0.3 \text{ cm}^{-3}$) warm ($T \sim 8000 \text{ K}$) gas. Such gas will likely contain C II and H I, but very little C I and H_2 . This is because the formation rates of C I and H_2 are proportional to n^2 , while the destruction rates are proportional to n and thus the abundance drops in lower density gas. In addition, at high temperatures the C^+ recombination rates fall. The H_2 formation rate may also be lower in the WNM because at high temperatures the H I atoms colliding with grains will more likely bounce than stick (Burke & Hollenbach 1983). We tested results for an $A_V = 0.1$ cloud with $G_0 = 5.1$ and $n = 30 \text{ cm}^{-3}$ in which half the column is WNM gas. Here we have included the density and temperature effects in the rates but not reduced R due to a smaller sticking coefficient (see Fig. 12 arrow ‘W’). The model point which includes WNM moves towards lower $N_{\text{CI}}/N_{\text{CII}}$ ratio (by a factor of ~ 2) and lower f_{H_2} (by a factor of ~ 10). Part of the drop in f_{H_2} is due to lower H_2 self-shielding in the $n = 30 \text{ cm}^{-3}$ cloud. The resulting vector moves away from the low A_V observations, and along a path which is nearly parallel to the standard models. Because the addition of WNM along the line-of-sight only moves points parallel to the standard models, it is unlikely that the presence of a WNM component can explain the f_{H_2} and $N_{\text{CI}}/N_{\text{CII}}$ results at low column.

We next consider the effects of a higher cosmic ray ionization rate along low column density lines of sight. The effects of increasing the primary ionization rate by a factor of 10 has little affect on the H_2 columns since photodissociation dominates the destruction of H_2 . The $N_{\text{CI}}/N_{\text{CII}}$ ratio increases slightly (by $\sim 30\%$) due to the greater electron abundance from cosmic ray ionizations (Fig. 12 arrow ‘C’). We conclude that neither WNM nor enhanced cosmic ray rates can explain the low A_V observations.

Another possibility is that the low A_V lines of sight are strongly affected by grain processing in interstellar shocks. Jones et al. (1996) demonstrated that sputtering and grain-grain collisions can vaporize grains, and reduce the grain surface area in sufficiently fast $v_s \lesssim 150 \text{ km s}^{-1}$ shocks. In the interstellar medium, shock speeds tend to scale with $n^{-1/2}$,

so that lower density gas will experience higher velocity shocks. Low A_V gas may have higher fractions of low density WNM gas. We note however, that shocks of speeds $v_s \approx 100 \text{ km s}^{-1}$ tend to shatter the larger grains and produce a large population of small grains which increases the surface area. We speculate that another type of grain processing occurring in shocks is to sputter the surfaces “clean” and thereby modify the characteristics of the atomic hydrogen adsorption sites (e.g., binding energy).

A final possibility is that the low A_V columns are lines of sight which graze the edges of larger clouds. In this case, the typical shielding column density (which is weighted towards the smallest column direction, i.e., perpendicular to the line-of-sight) is much less than the line-of-sight column that we measure. We examine this possibility with a simple test. We take a cloud with a total $A_V = 1$ through the center and consider a ray which passes through the cloud with a column of $A_V = 0.1$. At the midpoint, such a ray passes through a minimum depth of $A_V = 2.5 \times 10^{-3}$ measured from the cloud surface. We take the n_{H_2} , n_{HI} , n_{CI} , and n_{CII} abundances as a function of cloud radius from model runs for $A_V = 1$, $G_0 = 5.1$, and $n = 30 \text{ cm}^{-3}$. We then integrate the N_{HI} , N_{H_2} , N_{CI} , and N_{CII} column densities along the grazing line of sight. Results are shown in Figure 12 as an arrow labeled ‘G’. We see that compared to an $A_V = 0.1$ cloud, the f_{H_2} decreases due to the diminished H_2 self-shielding at the cloud edge. Only a small molecular column exists between the FUV illuminated surface and points along the ray and thus the self-shielding is ineffective and the H_2 is dissociated. We also see that the $N_{\text{CI}}/N_{\text{CII}}$ ratio rises. This is because the FUV field is lower by a factor of two compared to the $A_V = 0.1$ cloud since the radiation can not penetrate from the backside of the larger cloud. The lower field reduces the photoionization rate of C to C^+ and increases the abundance of PAH^- which converts C^+ to C. (The lower field also reduces the H_2 dissociation rate but this reduction is offset by the lack of H_2 self-shielding). The results significantly move the model points towards the observations. We consider grazing incident lines of sight a potential explanation for the low column density observations without resorting to unusual grain properties.

For $A_V \lesssim 0.25$ we find two lines of sight to be anomalous. These are $\epsilon \text{ Per}$ ($A_V = 0.16$, $f_{\text{H}_2} = 0.20$) and 59 Cyg ($A_V = 0.11$, $f_{\text{H}_2} = 0.19$). These lines of sight have molecular fractions which are $\gtrsim 10^3$ times greater than others with similar (low) column densities and require different rates or environments than the low f_{H_2} cases. Including $\epsilon \text{ Per}$ and 59 Cyg in the χ^2 tests for the $0.03 \lesssim A_V \lesssim 0.25$, $N_{\text{H}_2} < 10^{17}$ sources raises the minimum χ^2 from 1.6 to 9.2 and thus these sources can well be considered to be part of a separate population than the rest of the low A_V and low f_{H_2} lines of sight. The $\kappa \text{ Ori}$ line of sight at slightly higher column density ($A_V = 0.17$) is part of the low f_{H_2} group as are $\epsilon \text{ Ori}$ ($A_V = 0.14$) and 15 Mon ($A_V = 0.13$). One explanation for these peculiar sight lines could be that shocks of speeds $v_s \approx 100 \text{ km s}^{-1}$ have significantly increased the population of small grains. The

resulting increase in grain surface area will increase the FUV extinction (and decrease the H₂ photodissociation rate) and also increase the H₂ formation rate. We find that with the FUV extinction and H₂ formation rate a factor of three higher than normal we can reproduce the $N_{\text{CI}}/N_{\text{CII}}$ ratio and molecular fraction for the ϵ Per line of sight. Unfortunately, there are no low resolution IUE data for ϵ Per to examine the FUV rise in the extinction curve. We also note that 59 Cyg is a variable Be star and column densities for this line of sight are highly uncertain (D. Massa, private communication).

4.5. $A_V > 0.25$ Lines of Sight

At columns densities $A_V > 0.25$ we found two points to be anomalous: 23 Ori and π Sco. Weingartner & Draine (2001) modeled the line of sight towards 23 Ori and found that they had some difficulty matching the high N_{CI} column even when recombination on grains was included. They proposed several additional processes which might be working to enhance the C abundance including the dissociative recombination of CH⁺. The CH⁺ abundance can be enhanced compared to normal equilibrium chemistry due to the effects of non-thermal chemistry (Flower & Pineau des Forets 1998; Joulain et al. 1998; Zsargó & Federman 2003). If turbulent velocities are sufficiently large ($v \gtrsim 3 - 4 \text{ km s}^{-1}$) and turbulent dissipation can drive reactions with temperature barriers, then a large column of CH⁺ can be produced (Joulain et al. 1998).

Another process which might account for the anomalous columns is the time dependence of the chemistry. The line of sight towards 23 Ori shows a large $N_{\text{CI}}/N_{\text{CII}}$ ratio at small molecular fractions f_{H_2} compared to the equilibrium abundances. Consider a parcel of gas which has been recently shocked (i.e., H₂ dissociated and C I ionized). The molecular hydrogen is produced at a rate of $\sim 3 \times 10^{-17} n^2 \text{ s}^{-1}$. The time to double the current fractional abundance $n_{\text{H}_2}/n \sim 5 \times 10^{-3}$ is about $t \sim 5 \times 10^{-3}/(3 \times 10^{-17} n) \text{ s}$ or $t \sim 5.3 \times 10^4 \text{ yr}$ for $n = 100 \text{ cm}^{-3}$. On the other hand, the time to double the current ratio $N_{\text{CI}}/N_{\text{CII}} \sim 0.01$ is about $t \sim 0.01/(\Phi_{\text{PAH}} 2.4 \times 10^{-7} n_{\text{PAH}^-}) \text{ s}$ or $t \sim 62 \text{ yr}$ for $n = 100 \text{ cm}^{-3}$, where we have used C⁺ recombination with PAH⁻, $\Phi_{\text{PAH}} = 0.5$, and n_{PAH^-} from equation (B14). The time to reach the equilibrium $N_{\text{CI}}/N_{\text{CII}}$ ratio is much shorter than the time to reach the equilibrium f_{H_2} fraction. Thus, for a recent ($t \lesssim 5 \times 10^4 \text{ yr}$) passage of a shock, the $N_{\text{CI}}/N_{\text{CII}}$ ratio has had time to reach equilibrium while the H₂ fraction is dissociated compared to equilibrium.

For π Sco consider a parcel of molecular gas which has been recently illuminated by a source of FUV radiation. The time to dissociate the current $f_{\text{H}_2} \sim 0.01$ at cloud center is $t \sim (G_0 I \beta [N_{\text{H}_2}] \exp[-2.5 A_V])^{-1}$ or $t \sim 1.1 \times 10^6 \text{ yr}$, where we have used $G_0 = 5.1$, $N_{\text{H}_2} = 1 \times 10^{19} \text{ cm}^{-2}$, $\beta[1 \times 10^{19} \text{ cm}^{-2}] = 1.7 \times 10^{-4}$ (Eq.[B3]), and $A_V = 0.13$. The time to

ionize the current $N_{\text{CI}}/N_{\text{CII}} \sim 10^{-4}$ ratio is about $t \sim (2.1 \times 10^{-10} G_0 \exp[-2.6 A_V])^{-1}$ s or $t \sim 41$ yr. Thus for a molecular clump illuminated within the past $\sim 10^6$ yr, the $N_{\text{CI}}/N_{\text{CII}}$ ratio is in equilibrium while the H_2 fraction is much higher than its equilibrium value.

One complicating factor which we have not yet considered is the effects of multiple clump components along the line of sight. In general, taking the observed column density and splitting it up into multiple clouds exposes more surfaces to the interstellar radiation field. In the case of optically thick clumps, this will decrease the $N_{\text{CI}}/N_{\text{CII}}$ ratio and decrease the molecular fraction f_{H_2} . For the case of optically thin clumps, the $N_{\text{CI}}/N_{\text{CII}}$ ratio will not change but f_{H_2} will drop due to reduced self-shielding. However, the effects of multiple clumps is important only for components of approximately equal column density. If one component dominates then the remaining smaller components do not contribute much to the total column. Since in general, the UV absorption spectroscopy observations are dominated by a single component, our neglect of multiple clouds should not significantly alter our results.

5. Summary

We have carried out an analysis of observations of the C I, C II, H I, and H_2 column densities in the diffuse ISM towards 42 lines of sight spanning a range of column densities $0.03 \leq A_V \leq 2.13$. We have fitted these columns using a 2-sided PDR model which simultaneously solves for the thermal and chemical balance throughout the layer. The relative columns of H I and H_2 are dependent on the rate coefficient R for H_2 formation on grain surfaces, on the ratio G_0/n , and on the total column N (or A_V) of the illuminated cloud. The relative columns of C I and C II depend on the electron and PAH abundances, the rate coefficients for neutralization of C^+ with PAHs (or Φ_{PAH}), the total column in the illuminated cloud, and G_0/n . Observations set the total columns of each line of sight plus the fractional abundances of H, H_2 , C, and C^+ . Our PDR models self consistently determine the electron, PAH^+ , PAH, and PAH^- abundances for each model. We have performed a χ^2 test using R , Φ_{PAH} , and G_0/n as our free parameters to find the best fits to the fractional abundances along each line of sight.

The results are shown in Figures 5 through 10, where we show the χ^2 contours in the R , Φ_{PAH} plane, given the best fitting G_0/n for each individual line of sight. Note that Figures 5 through 10 are the χ^2 for these values of R , Φ_{PAH} for all 42 sources. Our main conclusions are as follows:

1. For low column ($A_V < 0.25$) lines of sight, and for the low molecular columns and fractions

that accompany them ($N_{\text{H}_2} < 10^{17} \text{ cm}^{-2}$, $f_{\text{H}_2} < 10^{-4}$), we find $R \simeq 1 \times 10^{-17} \text{ cm}^3 \text{ s}^{-1}$ and $\Phi_{\text{PAH}} \sim 0.2 - 0.4$.

2. At higher column densities ($0.25 < A_V < 2.13$), we find $R \simeq 3.5 \times 10^{-17} \text{ cm}^3 \text{ s}^{-1}$ and $\Phi_{\text{PAH}} \sim 0.4$.

3. Our χ^2 fits show a correlated range of Φ_{PAH} and R values that provide as good fits as our “best fits” quoted above. For $A_V > 0.25$, we find good fits for $\Phi_{\text{PAH}} = 0.22(R/10^{-17} \text{ cm}^3 \text{ s}^{-1}) - 0.40$ as long as $R > 3 \times 10^{-17} \text{ cm}^3 \text{ s}^{-1}$. Very high values of R (or therefore Φ_{PAH}), however, can only be fit with very low average densities in the clouds along the 42 sight lines. Figure 10 shows that for densities (equivalently thermal pressures) thought to be typical of local diffuse interstellar clouds, a value of $R \sim 3.5 \times 10^{-17} \text{ cm}^3 \text{ s}^{-1}$ (and therefore $\Phi_{\text{PAH}} \sim 0.4$) is preferred. This value is consistent with previous determinations of R made by comparing observations of H_2 with model calculations (e.g., Jura 1975).

4. The low values of R for low column density sight lines may indicate shock processing that decreases grain surface area or modifies grain surfaces along these sightlines, thereby reducing the H_2 formation rates, or a line of sight which grazes a larger cloud.

5. Our results for Φ_{PAH} indicate that the crude estimates of these ratios adopted by Wolfire et al. (2003) were roughly correct. They confirm the importance of PAHs in determining the ionization level of atomic ions (in this case C vs C^+) in interstellar clouds.

M.G.W. was supported in part by a NASA Long Term Space Astrophysics (LTSA) grant NNG05GD64G. We thank an anonymous referee for a careful reading of our paper and for comments that improved the presentation.

A. Chemical Rates

The chemical rates with PAHs were presented in Wolfire et al. (2003) Appendix C2 for reactions involving the ionization balance of hydrogen. Here we reproduce the rates along with the Carbon rates used in this paper. Our starting point are the rates from Draine & Sutin (1987) with $N_C = 35$ carbon atoms, and disk PAHs with a radius $a = (N_C/1.222)^{0.5}$. We use a PAH abundance of $n_{\text{PAH}} = 6 \times 10^{-7}n$. Wolfire et al. (2003) introduced the factor Φ_{PAH} to account for a wide range of unknowns in the PAH distribution and rate coefficients. Simple fits to the rates appropriate to diffuse ISM conditions are presented in Table 2.

B. Estimating Radiation Field G_0 and Density n

In this appendix we derive simple expressions to estimate the FUV radiation field G_0 incident on the cloud and the cloud density n from the observed column densities of $N(\text{HI})$, N_{H_2} , N_{CI} , and N_{CII} . In the limit of no dust extinction, the equilibrium abundance of H_2 is given by

$$G_0 I n_{\text{H}_2} \beta[N_{\text{H}_2}] = R n n_{\text{HI}} \quad , \quad (\text{B1})$$

where G_0 is the incident FUV radiation field, I the unshielded photodissociation rate, $\beta[N_{\text{H}_2}]$ is the H_2 self-shielding factor, and R is the formation rate on grains. For H_2 columns $\lesssim 10^{14} \text{ cm}^{-2}$, $\beta[N_{\text{H}_2}] = 1$ and the molecular fraction is given by

$$f_{\text{H}_2} = \frac{2nR}{G_0 I} \quad . \quad (\text{B2})$$

To estimate G_0 and n we use a simple expression for the H_2 self-shielding formula from Draine & Bertoldi (1996)

$$\beta[N_{\text{H}_2}] = \left[\frac{N_0}{N_{\text{H}_2} + N_0} \right]^{3/4} \quad , \quad (\text{B3})$$

where $N_0 = 1 \times 10^{14} \text{ cm}^{-2}$ is the H_2 column where line self-shielding starts to become significant. We can integrate equation (B1) through the cloud

$$G_0 I N_0^{3/4} \int \frac{dN'_{\text{H}_2}}{[N_0 + N'_{\text{H}_2}]^{3/4}} = R n \int dN'_{\text{HI}} \quad . \quad (\text{B4})$$

Letting $x = N_0 + N_{\text{H}_2}$ the integral becomes

$$G_0 I N_0^{3/4} \int_{N_0}^{N_0 + N_{\text{H}_2}} \frac{dx'}{x'^{3/4}} = R n N_{\text{HI}} \quad . \quad (\text{B5})$$

Carrying out the integral and solving for G_0/n we have

$$\frac{G_0}{n} = \frac{0.25 N_{\text{HI}}}{\left\{ [N_0 + N_{\text{H}_2}]^{1/4} - N_0^{1/4} \right\} N_0^{3/4} I} \frac{R}{I} \quad , \quad (\text{B6})$$

or

$$\frac{G_0}{n} = \mathcal{X}_{\text{H}} \frac{R}{I} \quad , \quad (\text{B7})$$

with

$$\mathcal{X}_{\text{H}} = \frac{0.25 N_{\text{HI}}}{\left\{ [N_0 + N_{\text{H}_2}]^{1/4} - N_0^{1/4} \right\} N_0^{3/4}} \quad . \quad (\text{B8})$$

For $N_{\text{H}_2} > N_0$ from equations (B7), (B8) and Hollenbach & Tielens (1999) the molecular fraction is given by

$$f_{\text{H}_2} = 2 \left(\frac{Rn}{4G_0I} \right)^4 \left(\frac{N}{N_0} \right)^3 . \quad (\text{B9})$$

For clouds where the optical depth of the dust becomes significant the local FUV field within the cloud is less than the incident field. We assume the flux on each side of a slab is $1/2G_0$ and the mean field, $\langle G_0 \rangle$ within the slab is approximately at a depth of $1/4$ the total column density or at a depth of $1/4A_V$. Thus the mean field is given by

$$\langle G_0 \rangle = \frac{1}{2}G_0e^{(-\frac{3}{4}\alpha A_V)} + \frac{1}{2}G_0e^{(-\frac{1}{4}\alpha A_V)} , \quad (\text{B10})$$

where $\alpha = 2.5$ converts the FUV extinction at visual wavelengths to optical depth at the FUV dissociation energies of H_2 . Solving for G_0 we have

$$G_0 = \frac{2\langle G_0 \rangle e^{\frac{2.5}{4}A_V}}{1 + e^{-\frac{2.5}{2}A_V}} . \quad (\text{B11})$$

Setting G_0 in equation (B7) to the mean field $\langle G_0 \rangle$ we have

$$\frac{G_0}{n} = \frac{2e^{\frac{2.5}{4}A_V}}{1 + e^{-\frac{2.5}{2}A_V}} \mathcal{X}_{\text{H}} \frac{R}{I} . \quad (\text{B12})$$

The analytic solution is approximate since $1/4A_V$ is an approximation to the depth where the local field equals the mean field. Comparing equation (B12) with our numerical results we find we can achieve better agreement with an additional factor of $1/2$ on the right hand side.

A second estimate of G_0/n can be obtained from the $N_{\text{CI}}/N_{\text{CII}}$ ratio. There are several destruction processes for C^+ to consider depending on the PAH^- abundance. If destruction occurs primarily through recombination on PAH^- then the equilibrium abundance of C^0 is found by balancing recombination with photoionization of C

$$G_0I_{\text{C}}n_{\text{C}^0} = \Phi_{\text{PAH}}\kappa_1n_{\text{C}^+}n_{\text{PAH}^-} , \quad (\text{B13})$$

where $G_0I_{\text{C}} = G_02.1 \times 10^{-10} \text{ s}^{-1}$ is the photoionization rate of C^0 , and $\Phi_{\text{PAH}}\kappa_1 = \Phi_{\text{PAH}}2.4 \times 10^{-7}T_2^{-0.5} \text{ cm}^3 \text{ s}^{-1}$ is the C^+ recombination rate with PAH^- . From Wolfire et al. (2003), the PAH^- abundance in the regime $n_{\text{PAH}^-}/n_{\text{PAH}^0} < 1$ is given by

$$n_{\text{PAH}^-} = 4.8 \times 10^{-5}n_en\Phi_{\text{PAH}}G_0^{-1} \text{ cm}^{-3}, \quad (\text{B14})$$

with the electron density n_e and hydrogen nucleus density n in units of cm^{-3} . Substituting this expression for n_{PAH^-} into equation (B13), and solving for G_0/n we have

$$\frac{G_0}{n} = 4.1 \times 10^{-3} \Phi_{\text{PAH}} T_2^{-0.25} \left[\frac{N_{\text{CI}}}{N_{\text{CII}}} \right]^{-1/2} \quad (\text{B15})$$

where we have used an electron abundance of $n_e \approx 3 \times 10^{-4} n \text{ cm}^{-3}$ (including metals, especially ionization of C, and ionization of H by soft X-rays), and substituted the observed ratio $N_{\text{CI}}/N_{\text{CII}}$ for $n_{\text{C}^0}/n_{\text{C}^+}$.

If the abundance of PAH^- is low enough, then the destruction of C^+ occurs through charge exchange with PAH^0 or through electron recombination in the gas phase. The equilibrium abundance is then given by

$$G_0 I_{\text{C}} n_{\text{C}^0} = n_{\text{C}^+} (k_2 n_{\text{PAH}^0} + k_3 n_e) \quad (\text{B16})$$

with $k_2 = 8.8 \times 10^{-9} \Phi_{\text{PAH}} \text{ cm}^3 \text{ s}^{-1}$, and $k_3 = 1.8 \times 10^{-11} T_2^{-0.83} \text{ cm}^3 \text{ s}^{-1}$. Using the PAH^0 abundance of ~ 0.7 times the total PAH abundance ($n_{\text{PAH}^0} = 0.7 \times 6 \times 10^{-7} n$; Wolfire et al. 2003), and an electron abundance of $n_e \approx 3 \times 10^{-4} n \text{ cm}^{-3}$, we can solve for G_0/n

$$\frac{G_0}{n} = (1.8 \times 10^{-5} \Phi_{\text{PAH}} + 2.6 \times 10^{-5} T_2^{-0.83}) \left[\frac{N_{\text{CI}}}{N_{\text{CII}}} \right]^{-1} \quad (\text{B17})$$

We find that the destruction of C^+ by PAH^0 dominates at a limit of approximately

$$\frac{G_0}{n} \gtrsim \frac{T_2^{-1/2} \Phi_{\text{PAH}}^2}{1.2 \Phi_{\text{PAH}} + 1.6 T_2^{-0.83}} \quad (\text{B18})$$

From equation (B15), and setting $T_2 = 1$, and $\Phi_{\text{PAH}} = 0.5$, this limit corresponds to an observed column density ratio $N_{\text{CI}}/N_{\text{CII}} \lesssim 3 \times 10^{-4}$. Thus for $N_{\text{CI}}/N_{\text{CII}} \lesssim 3 \times 10^{-4}$ we use equation (B17) while for $N_{\text{CI}}/N_{\text{CII}} \gg 3 \times 10^{-4}$ we use equation (B15).

Similar to the G_0/n estimate based on H_2 columns we also correct the incident FUV field for dust extinction within the cloud by setting the G_0 in equations (B15) and (B17) to the mean FUV field $\langle G_0 \rangle$ and solve for the extinction corrected G_0/n . In solving for the minimum χ^2 , we use the estimates for G_0/n presented here along with a fixed value of $G_0 = 1.7$ to provide a first guess range of n . If the minimum in χ^2 is not crossed within the first range of n we take a second range given by $n_{\text{max}} \times (n_{\text{max}}/n_{\text{min}})$ if higher densities are required or $n_{\text{min}} \times (n_{\text{max}}/n_{\text{min}})^{-1}$ if lower densities are required (where n_{max} and n_{min} refer to the maximum and minimum densities in the range). The minimum in χ^2 is generally found within the first or second range. We then do a quadratic fit of the χ^2 values as a function of density to find the density which provides the minimum χ^2 value.

C. Variation of $N_{\text{CI}}/N_{\text{CII}}$ as a function of G_0/n and Φ_{PAH}

In Figures 1 through 4 we show the variation in $N_{\text{CI}}/N_{\text{CII}}$ versus f_{H_2} as a function of G_0/n and Φ_{PAH} . In the limit of low G_0/n the destruction of C^+ is dominated by recombination on PAH^- and rate equation (B13) applies. From equation (B15) we have

$$\frac{N_{\text{CI}}}{N_{\text{CII}}} \propto \Phi_{\text{PAH}}^2 \left[\frac{n}{G_0} \right]^2 . \quad (\text{C1})$$

We see in Figures 1 through 4, along curves of constant G_0 , the $N_{\text{CI}}/N_{\text{CII}}$ ratio rises steeply as n increases.

In the limit of high G_0/n the destruction of C^+ is dominated by charge exchange with PAH^0 and rate equation (B16) applies. From equation (B17) the $N_{\text{CI}}/N_{\text{CII}}$ ratio is given by

$$\frac{N_{\text{CI}}}{N_{\text{CII}}} \propto \Phi_{\text{PAH}} \left[\frac{n}{G_0} \right] , \quad (\text{C2})$$

and the curves start to flatten as n decreases.

At low values of Φ_{PAH} the destruction of C^+ is dominated by gas phase recombination with electrons, n_e . In the limit of low values of G_0/n , the electron abundance is determined mainly by the photoionization and recombination of Carbon. From equation (B17) the $N_{\text{CI}}/N_{\text{CII}}$ ratio is given by

$$\frac{N_{\text{CI}}}{N_{\text{CII}}} \propto \left[\frac{n}{G_0} \right] . \quad (\text{C3})$$

In the limit of high G_0/n , the electron abundance is mainly determined by the soft X-ray photoionization of H. In this case $n_e \propto n^{1/2}$ and

$$\frac{N_{\text{CI}}}{N_{\text{CII}}} \propto \frac{n^{1/2}}{G_0} , \quad (\text{C4})$$

and we see that the curves flatten considerably at low values of n .

REFERENCES

- Abgrall, H., Le Bourlot, J., Pineau Des Forets, G., Roueff, E., Flower, D. R., & Heck, L. 1992, A&A, 253, 525
- Altun, Z., Yumak, A., Badnell, N. R., Colgan, J., & Pindzola, M. S. 2004, A&A, 420, 775
- Bakes, E. L. O., & Tielens, A. G. G. M. 1998, ApJ, 499, 258

- Boissé, P., Le Petit, F., Rollinde, E., Roueff, E., Pineau des Forêts, G., Andersson, B.-G., Gry, C., & Felenbok, P. 2005, *A&A*, 429, 509
- Bohlin, R. C., Savage, B. D., & Drake, J. F. 1978, *ApJ*, 224, 132
- Browning, M. K., Tumlinson, J., & Shull, J. M. 2003, *ApJ*, 582, 810
- Burke, J. R., & Hollenbach, D. J. 1983, *ApJ*, 265, 223
- Cartledge, S. I. B., Lauroesch, J. T., Meyer, D. M., & Sofia, U. J. 2004, *ApJ*, 613, 1037
- Cazaux, S., & Tielens, A. G. G. M. 2004, *ApJ*, 604, 222
- Chang, Q., Cuppen, H. M., & Herbst, E. 2006, *A&A*, 458, 497
- Diplas, A., & Savage, B. D. 1994, *ApJS*, 93, 211
- Draine, B. T. 1978, *ApJS*, 36, 595
- Draine, B. T., & Bertoldi, F. 1996, *ApJ*, 468, 269
- Draine, B. T., & Sutin, B. 1987, *ApJ*, 320, 803
- Fitzpatrick, E. L., & Massa, D. 1990, *ApJS*, 72, 163
- Flower, D. R., & Pineau des Forets, G. 1998, *MNRAS*, 297, 1182
- Gillmon, K., & Shull, J. M. 2006, *ApJ*, 636, 908
- Gry, C., Boulanger, F., Nehmé, C., Pineau des Forêts, G., Habart, E., & Falgarone, E. 2002, *A&A*, 391, 675
- Habart, E., Boulanger, F., Verstraete, L., Walmsley, C. M., & Pineau des Forêts, G. 2004, *A&A*, 414, 53
- Habing, H. J. 1968, *Bull. Astron. Inst. Netherlands*, 19, 421
- Hobbs, L. M., York, D. G., & Oegerle, W. 1982, *ApJ*, 252, L21
- Hollenbach, D. J., & Tielens, A. G. G. M. 1999, *Reviews of Modern Physics*, 71, 173
- Hollenbach, D., & Salpeter, E. E. 1971, *ApJ*, 163, 155
- Howk, J. C., Savage, B. D., & Fabian, D. 1999, *ApJ*, 525, 253
- Jenkins, E. B., Jura, M., & Loewenstein, M. 1983, *ApJ*, 270, 88

- Jenkins, E. B., & Shaya, E. J. 1979, *ApJ*, 231, 55
- Jenkins, E. B., & Tripp, T. M. 2001, *ApJS*, 137, 297
- Jenkins, E. B., & Peimbert, A. 1997, *ApJ*, 477, 265
- Jenkins, E. B., Tripp, T. M., Woźniak, P. R., Sofia, U. J., & Sonneborn, G. 1999, *ApJ*, 520, 182
- Jenkins, E. B., Woźniak, P. R., Sofia, U. J., Sonneborn, G., & Tripp, T. M. 2000, *ApJ*, 538, 275
- Jones, A. P., Tielens, A. G. G. M., & Hollenbach, D. J. 1996, *ApJ*, 469, 740
- Joulain, K., Falgarone, E., Des Forets, G. P., & Flower, D. 1998, *A&A*, 340, 241
- Jura, M. 1975, *ApJ*, 197, 575
- Kaufman, M. J., Wolfire, M. G., Hollenbach, D. J., & Luhman, M. L. 1999, *ApJ*, 527, 795
- Le Petit, F., Nehmé, C., Le Bourlot, J., & Roueff, E. 2006, *ApJS*, 164, 506
- Lepp, S., Dalgarno, A., van Dishoeck, E. F., & Black, J. H. 1988, *ApJ*, 329, 418
- Lipshtat, A., & Biham, O. 2003, *A&A*, 400, 585
- McCall, B. J., et al. 2003, *Nature*, 422, 500
- Nahar, S. N., & Pradhan, A. K. 1997, *ApJS*, 111, 339
- Neufeld, D. A., Wolfire, M. G., & Schilke, P. 2005, *ApJ*, 628, 260
- Péquignot, D. 1990, *A&A*, 231, 499 (erratum 313, 1026 [1996])
- Pirronello, V., Liu, C., Roser, J. E., & Vidali, G. 1999, *A&A*, 344, 681
- Rachford, B. L., et al. 2002, *ApJ*, 577, 221
- Savage, B. D., Bohlin, R. C., Drake, J. F., & Budich, W. 1977, *ApJ*, 216, 291
- Shull, J. M., & van Steenberg, M. E. 1985, *ApJ*, 294, 599
- Snow, T. P., Jr. 1977, *ApJ*, 216, 724
- Snow, T. P., Black, J. H., van Dishoeck, E. F., Burks, G., Crutcher, R. M., Lutz, B. L., Hanson, M. M., & Shuping, R. Y. 1996, *ApJ*, 465, 245

- Snow, T. P., & McCall, B. J. 2006, *ARA&A*, 44, 367
- Sofia, U. J., Lauroesch, J. T., Meyer, D. M., & Cartledge, S. I. B. 2004, *ApJ*, 605, 272
- Sonnentrucker, P., Friedman, S. D., Welty, D. E., York, D. G., & Snow, T. P. 2002, *ApJ*, 576, 241
- Sonnentrucker, P., Friedman, S. D., Welty, D. E., York, D. G., & Snow, T. P. 2003, *ApJ*, 596, 350
- Snow, T. P., Hanson, M. M., Black, J. H., van Dishoeck, E. F., Crutcher, R. M., & Lutz, B. L. 1998, *ApJ*, 496, L113
- Taylor, J. R. 1997, *The Study of Uncertainties in Physical Measurements*, (Mill Valley: University Science Books)
- Wannier, P., Andersson, B.-G., Penprase, B. E., & Federman, S. R. 1999, *ApJ*, 510, 291
- Weingartner, J. C., & Draine, B. T. 2001, *ApJ*, 563, 842
- Welty, D. E., Hobbs, L. M., & Morton, D. C. 2003, *ApJS*, 147, 61
- Wolfire, M. G., Hollenbach, D., McKee, C. F., Tielens, A. G. G. M., & Bakes, E. L. O. 1995, *ApJ*, 443, 152
- Wolfire, M. G., McKee, C. F., Hollenbach, D., & Tielens, A. G. G. M. 2003, *ApJ*, 587, 278
- Zsargó, J., & Federman, S. R. 2003, *ApJ*, 589, 319
- Zsargo, J., Federman, S. R., & Cardelli, J. A. 1997, *ApJ*, 484, 820

Table 1. Observations

| Star | | $\log N_{\text{HI}}$ (cm^{-2}) | $\log N_{\text{H}_2}$ (cm^{-2}) | $\log N_{\text{CI}}$ (cm^{-2}) | $\log N_{\text{CII}}$ (cm^{-2}) | A_V | $\log f_{\text{H}_2}^{\text{a}}$ | $\log f_{\text{CI}}^{\text{b}}$ | References |
|----------------|-----------|--|---|--|---|-------|----------------------------------|---------------------------------|---------------|
| κ Cas | HD 2905 | 21.21 ± 0.11 | 20.27 ± 0.18 | 15.55 ± 0.20 | 17.50 ± 0.22 | 0.98 | -0.73 | -1.95 | 1, 2, 7 |
| 40 Per | HD 22951 | 21.05 ± 0.11 | 20.46 ± 0.18 | 15.25 ± 0.06 | $17.43 \pm 0.11^{\text{b}}$ | 0.85 | -0.47 | -2.18 | 1, 2, 3 |
| o Per | HD 23180 | 20.91 ± 0.11 | 20.61 ± 0.15 | 15.68 ± 0.06 | 17.41 ± 0.11 | 0.79 | -0.30 | -1.73 | 1, 2, 3 |
| ζ Per | HD 24398 | 20.81 ± 0.04 | 20.67 ± 0.10 | 15.52 ± 0.05 | $17.35 \pm 0.08^{\text{c}}$ | 0.79 | -0.23 | -1.83 | 3, 4, 5, 6 |
| χ Per | HD 24534 | 20.72 ± 0.06 | 20.92 ± 0.04 | 16.30 ± 0.20 | $17.53 \pm 0.14^{\text{c}}$ | 1.10 | -0.12 | -1.24 | 6, 17, 22, 24 |
| ξ Per | HD 24912 | 21.07 ± 0.06 | 20.53 ± 0.08 | 15.12 ± 0.14 | $17.51 \pm 0.13^{\text{c}}$ | 0.98 | -0.44 | -2.39 | 3, 4, 6, 7 |
| ϵ Per | HD 24760 | 20.42 ± 0.06 | 19.53 ± 0.15 | 13.71 ± 0.05 | 16.72 ± 0.07 | 0.16 | -0.69 | -3.01 | 4, 8 |
| | HD 34078 | $21.43 \pm 0, 10$ | 20.81 ± 0.03 | 16.24 ± 0.44 | 17.80 ± 0.45 | 2.00 | -0.49 | -1.56 | 27 |
| 23 Ori | HD 35149 | 20.74 ± 0.08 | 18.30 ± 0.11 | 14.99 ± 0.05 | 16.94 ± 0.09 | 0.28 | -2.14 | -1.95 | 4, 9, 10 |
| δ Ori | HD 36486 | 20.19 ± 0.03 | 14.74 ± 0.05 | 13.02 ± 0.09 | 16.39 ± 0.09 | 0.085 | -5.15 | -3.37 | 7, 11, 12 |
| λ Ori | HD 36861 | 20.79 ± 0.08 | 19.11 ± 0.11 | 14.32 ± 0.04 | $17.00 \pm 0.21^{\text{c}}$ | 0.32 | -1.40 | -2.68 | 4, 6, 8 |
| ι Ori | HD 37043 | 20.16 ± 0.05 | $14.69 \pm 0.20^{\text{d}}$ | 12.98 ± 0.14 | 16.36 ± 0.15 | 0.071 | -5.17 | -3.38 | 2, 4, 7 |
| ϵ Ori | HD 37128 | 20.46 ± 0.07 | 16.28 ± 0.20 | 13.59 ± 0.10 | 16.66 ± 0.12 | 0.14 | -3.88 | -3.07 | 4, 7, 12 |
| ζ Ori | HD 37742 | 20.41 ± 0.08 | 15.82 ± 0.20 | 13.88 ± 0.20 | 16.61 ± 0.22 | 0.13 | -4.29 | -2.73 | 1, 9, 10, 13 |
| μ Col | HD 38666 | 19.86 ± 0.08 | $15.51 \pm 0.20^{\text{d}}$ | 12.96 ± 0.03 | 16.06 ± 0.08 | 0.036 | -4.05 | -3.10 | 2, 23 |
| κ Ori | HD 38771 | 20.53 ± 0.04 | $15.68 \pm 0.20^{\text{d}}$ | 13.68 ± 0.08 | 16.73 ± 0.09 | 0.17 | -4.55 | -3.05 | 2, 4, 7 |
| 139 τ | HD 40111 | 20.90 ± 0.08 | 19.74 ± 0.20 | 14.23 ± 0.18 | 17.16 ± 0.19 | 0.46 | -0.92 | -2.93 | 1, 2, 7 |
| 15 Mon | HD 47839 | 20.36 ± 0.06 | $15.55 \pm 0.20^{\text{d}}$ | 13.40 ± 0.15 | 16.56 ± 0.16 | 0.13 | -4.51 | -3.16 | 4, 2, 14 |
| ζ Pup | HD 66811 | 19.99 ± 0.02 | $14.45 \pm 0.20^{\text{d}}$ | 13.26 ± 0.09 | 16.19 ± 0.09 | 0.049 | -5.24 | -2.93 | 1, 2, 14 |
| γ^2 Vel | HD 68273 | 19.78 ± 0.04 | $14.23 \pm 0.20^{\text{d}}$ | 13.12 ± 0.17 | 15.98 ± 0.17 | 0.031 | -5.25 | -2.86 | 1, 2, 14 |
| ρ Leo | HD 91316 | 20.26 ± 0.08 | $15.61 \pm 0.20^{\text{d}}$ | 13.33 ± 0.22 | 16.46 ± 0.23 | 0.091 | -4.35 | -3.13 | 1, 2, 14 |
| | HD 112244 | 21.08 ± 0.08 | 20.14 ± 0.11 | 14.69 ± 0.05 | 17.37 ± 0.08 | 0.74 | -0.73 | -2.68 | 1, 2, 8 |

Table 1—Continued

| | Star | $\log N_{\text{HI}}$ (cm^{-2}) | $\log N_{\text{H}_2}$ (cm^{-2}) | $\log N_{\text{CI}}$ (cm^{-2}) | $\log N_{\text{CII}}$ (cm^{-2}) | A_V | $\log f_{\text{H}_2}^{\text{a}}$ | $\log f_{\text{CI}}^{\text{b}}$ | References |
|----------------|------------|--|---|--|---|-------|----------------------------------|---------------------------------|-------------|
| 1 Sco | HD 141637 | 21.19 ± 0.08 | 19.23 ± 0.18 | 14.00 ± 0.05 | 17.40 ± 0.09 | 0.80 | -1.67 | -3.40 | 1, 2, 8 |
| π Sco | HD 143018 | 20.72 ± 0.04 | 19.32 ± 0.20 | 13.03 ± 0.05 | 16.95 ± 0.06 | 0.28 | -1.13 | -3.92 | 1, 2, 8 |
| δ Sco | HD 143275 | 21.14 ± 0.08 | 19.41 ± 0.20 | 14.25 ± 0.05 | 17.36 ± 0.09 | 0.74 | -1.45 | -3.11 | 1, 2, 8 |
| β^1 Sco | HD 144217 | 21.10 ± 0.04 | 19.83 ± 0.06 | 14.42 ± 0.06 | $17.37 \pm 0.10^{\text{c}}$ | 0.70 | -1.01 | -2.92 | 1, 2, 6, 15 |
| ω^1 Sco | HD 144470 | 21.18 ± 0.08 | 20.05 ± 0.11 | 14.35 ± 0.05 | 17.44 ± 0.09 | 0.88 | -0.89 | -3.09 | 1, 2, 8 |
| ν Sco | HD 145502 | 21.14 ± 0.15 | 19.89 ± 0.15 | 14.56 ± 0.27 | 17.39 ± 0.30 | 0.78 | -1.00 | -2.83 | 1, 2, 7 |
| σ Sco | HD 147165 | 21.34 ± 0.15 | 19.79 ± 0.15 | 14.38 ± 0.05 | 17.56 ± 0.15 | 1.15 | -1.27 | -3.18 | 1, 2, 8 |
| ρ Oph | HD 147933A | 21.55 ± 0.10 | 20.57 ± 0.15 | 15.52 ± 0.02 | 17.83 ± 0.09 | 2.13 | -0.76 | -2.31 | 2, 15, 16 |
| χ Oph | HD 148184 | 21.14 ± 0.08 | 20.63 ± 0.18 | 15.33 ± 0.01 | 17.55 ± 0.09 | 1.15 | -0.42 | -2.22 | 1, 2, 15 |
| 22 Sco | HD 148605 | 20.95 ± 0.08 | 18.74 ± 0.18 | 13.95 ± 0.50 | 17.16 ± 0.51 | 0.46 | -1.92 | -3.21 | 1, 2, 7 |
| ζ Oph | HD 149757 | 20.72 ± 0.02 | 20.65 ± 0.05 | 15.51 ± 0.07 | $17.36 \pm 0.11^{\text{c}}$ | 0.71 | -0.20 | -1.84 | 2, 4, 6 |
| | HD 154368 | 21.00 ± 0.05 | 21.16 ± 0.07 | 16.22 ± 0.20 | 17.79 ± 0.21 | 1.96 | -0.13 | -1.57 | 17, 18 |
| γ Ara | HD 157246 | 20.71 ± 0.06 | 19.24 ± 0.13 | 13.87 ± 0.12 | 16.94 ± 0.13 | 0.26 | -1.20 | -3.07 | 4, 7 |
| κ Aql | HD 184915 | 20.90 ± 0.11 | 20.31 ± 0.15 | 14.37 ± 0.16 | 17.28 ± 0.18 | 0.61 | -0.47 | -2.91 | 1, 2, 7 |
| | HD 185418 | 21.11 ± 0.15 | 20.76 ± 0.05 | 15.57 ± 0.09 | 17.59 ± 0.12 | 1.24 | -0.33 | -2.02 | 17, 25, 26 |
| | HD 192639 | 21.29 ± 0.09 | 20.69 ± 0.05 | 15.37 ± 0.08 | 17.67 ± 0.10 | 1.55 | -0.48 | -2.30 | 4, 17, 20 |
| 59 Cyg | HD 200120 | 20.25 ± 0.08 | 19.32 ± 0.18 | 13.94 ± 0.15 | 16.54 ± 0.17 | 0.11 | -0.72 | -2.60 | 1, 2, 7 |
| | HD 206267 | 21.31 ± 0.15 | 20.86 ± 0.04 | $15.30 \pm 0.08^{\text{e}}$ | 17.74 ± 0.12 | 1.74 | -0.38 | -2.44 | 17, 21 |
| | HD 210839 | 21.16 ± 0.10 | 20.84 ± 0.04 | 14.98 ± 0.08 | 17.65 ± 0.10 | 1.42 | -0.31 | -2.67 | 17, 21, 22 |
| σ Cas | HD 224572 | 20.88 ± 0.08 | 20.23 ± 0.18 | 14.74 ± 0.19 | 17.24 ± 0.21 | 0.55 | -0.51 | -2.50 | 1, 2, 7 |

References. — (1) Bohlin et al. (1978); (2) Savage et al. (1977); (3) Wannier et al. (1999); (4) Cartledge et al. (2004); (5) Snow (1977); (6) Sofia et al. (2004); (7) Jenkins et al. (1983); (8) Zsargó & Federman (2003); (9) Welty et al. (2003); (10) Compilation of column densities by D. Welty <http://astro.uchicago.edu/home/web/welty/coldens.html>; (11) Jenkins et al. (1999); (12) Jenkins et al. (2000); (13) Jenkins & Peimbert (1997); (14) Jenkins & Shaya (1979); (15) Zsargo et al. (1997); (16) Shull & van Steenberg (1985); (17) Rachford et al. (2002); (18) Snow et al. (1996); (19) Gry et al. (2002); (20) Sonnentrucker et al. (2002); (21) Jenkins & Tripp (2001); (22) Diplas & Savage (1994); (23) Howk et al. (1999); (24) Snow et al. (1998); (25) Fitzpatrick & Massa (1990); (26) Sonnentrucker et al. (2003); (27) Boissé et al. (2005)

$${}^a f_{\text{H}_2} = 2N_{\text{H}_2}/[N_{\text{HI}} + 2N_{\text{H}_2}].$$

$${}^b f_{\text{CI}} = N_{\text{CI}}/N_{\text{CII}}.$$

${}^b N_{\text{CII}}$ is taken as $1.6 \times 10^{-4} \times [N_{\text{HI}} + 2N_{\text{H}_2}]$ unless otherwise noted.

c Observed N_{CII} .

d Uncertainties for low N_{H_2} columns were not given in Savage et al. (1977). We use the uncertainty suggested by Welty [Reference (10)].

f C I column uncertainty assumed to be similar to Sonnentrucker et al. (2002).

Table 2. Reaction Rates

| Reaction | Rate ($\text{cm}^3 \text{s}^{-1}$) |
|---|---|
| $\text{PAH}^- + \text{H}^+ \rightarrow \text{PAH}^0 + \text{H}$ | $8.3 \times 10^{-7} \Phi_{\text{PAH}} T_2^{-0.5} \text{ }^{\text{a}}$ |
| $\text{PAH}^0 + \text{H}^+ \rightarrow \text{PAH}^+ + \text{H}$ | $3.1 \times 10^{-8} \Phi_{\text{PAH}}$ |
| $\text{PAH}^+ + e \rightarrow \text{PAH}^0$ | $3.5 \times 10^{-5} \Phi_{\text{PAH}} T_2^{-0.5}$ |
| $\text{PAH}^0 + e \rightarrow \text{PAH}^-$ | $1.3 \times 10^{-6} \Phi_{\text{PAH}}$ |
| $\text{PAH}^- + \text{C}^+ \rightarrow \text{PAH}^0 + \text{C}$ | $2.4 \times 10^{-7} \Phi_{\text{PAH}} T_2^{-0.5} \text{ }^{\text{b}}$ |
| $\text{PAH}^0 + \text{C}^+ \rightarrow \text{PAH}^+ + \text{C}$ | $8.8 \times 10^{-9} \Phi_{\text{PAH}} \text{ }^{\text{b}}$ |
| $\text{PAH}^0 + h\nu \rightarrow \text{PAH}^+ + e$ | $4.6 \times 10^{-9} G_0 \exp(-1.8A_V) \text{ }^{\text{c}}$ |
| $\text{PAH}^- + h\nu \rightarrow \text{PAH}^0 + e$ | $1.2 \times 10^{-8} G_0 \exp(-1.8A_V) \text{ }^{\text{c}}$ |
| $\text{C} + h\nu \rightarrow \text{C}^+ + e$ | $2.1 \times 10^{-10} G_0 \exp(-2.6A_V) \text{ }^{\text{c}}$ |
| $\text{C}^+ + e \rightarrow \text{C} + h\nu$ | $1.8 \times 10^{-11} T_2^{-0.83}$ |

^a $T_2 = T/100$ K.

^bAdditional collisional rates scale as $(m)^{-0.5}$ where m is the mass of the collision partner.

^cPhoto rates have units s^{-1} . G_0 is the FUV field measured in units of the Habing (1968) field ($= 1.6 \times 10^{-4} \text{ erg cm}^{-2} \text{ s}^{-1} \text{ sr}^{-1}$). The Draine (1978) field is a factor of 1.7 larger.

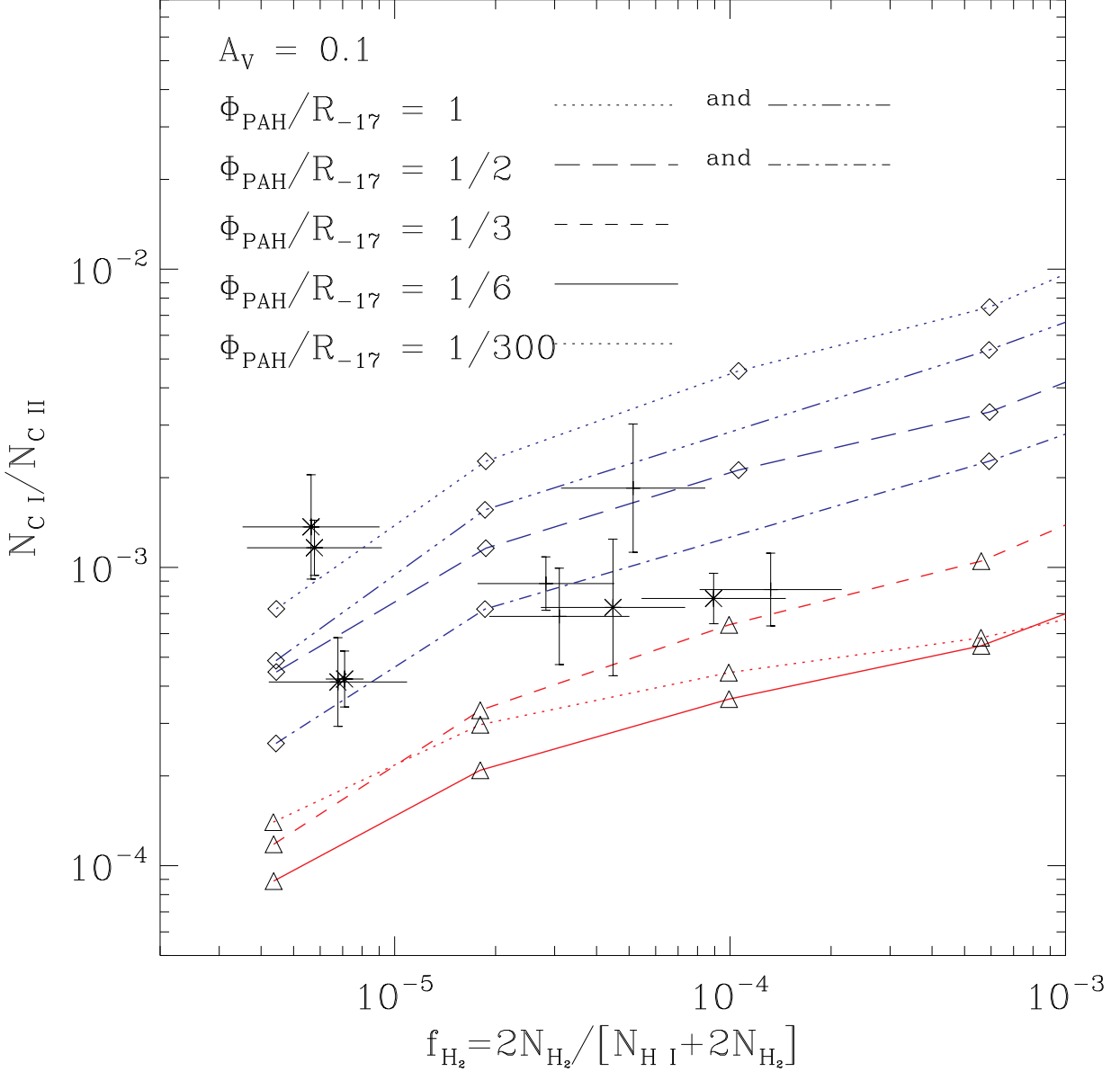


Fig. 1.— Column density ratio $N_{\text{C I}}/N_{\text{C II}}$ versus molecular hydrogen fraction $f_{\text{H}_2} = 2N_{\text{H}_2}/[N_{\text{H I}} + 2N_{\text{H}_2}]$. Observations are shown for cloud column densities in the range $0.03 \lesssim A_V \lesssim 0.25$, $N_{\text{H}_2} < 10^{17} \text{ cm}^{-2}$, and molecular fraction $f_{\text{H}_2} \lesssim 10^{-4}$. Clouds with $A_V < 0.1$ are indicated with an “x”. Curves show model results for cloud column $A_V = 0.1$, and various values of $\Phi_{\text{PAH}}/R_{-17}$ where $R_{-17} = R/10^{-17}$. $\Phi_{\text{PAH}} = 2.0$, $R = 2 \times 10^{-17} \text{ cm}^3 \text{ s}^{-1}$ ($\Phi_{\text{PAH}}/R = 1$; *dot*), $\Phi_{\text{PAH}} = 1$, $R = 1 \times 10^{-17} \text{ cm}^3 \text{ s}^{-1}$ ($\Phi_{\text{PAH}}/R = 1$; *dash-dot-dot*), $\Phi_{\text{PAH}} = 0.5$, $R = 1 \times 10^{-17} \text{ cm}^3 \text{ s}^{-1}$ ($\Phi_{\text{PAH}}/R = 1/2$; *long dash*), $\Phi_{\text{PAH}} = 1$, $R = 2 \times 10^{-17} \text{ cm}^3 \text{ s}^{-1}$ ($\Phi_{\text{PAH}}/R = 1/2$; *dash-dot*), $\Phi_{\text{PAH}} = 1$, $R = 3 \times 10^{-17} \text{ cm}^3 \text{ s}^{-1}$ ($\Phi_{\text{PAH}}/R = 1/3$; *short dash*), $\Phi_{\text{PAH}} = 0.5$, $R = 3 \times 10^{-17} \text{ cm}^3 \text{ s}^{-1}$ ($\Phi_{\text{PAH}}/R = 1/6$; *solid*), and $\Phi_{\text{PAH}} = 0.01$, $R = 3 \times 10^{-17} \text{ cm}^3 \text{ s}^{-1}$ ($\Phi_{\text{PAH}}/R = 1/300$; *dot*; lower curves). The ratio G_0/n varies along each model curve with higher G_0/n yielding smaller values of f_{H_2} . Individual models are shown with $n = 10, 20, 30$, and 40 cm^{-3} (with the exception of the *dash-dot* and *dash-dot-dot* curves where $n = 5, 10$, and 20 cm^{-3}) and $G_0 = 1.7$ (\diamond ; *Blue*) and $G_0 = 5.1$ (\triangle ; *Red*).

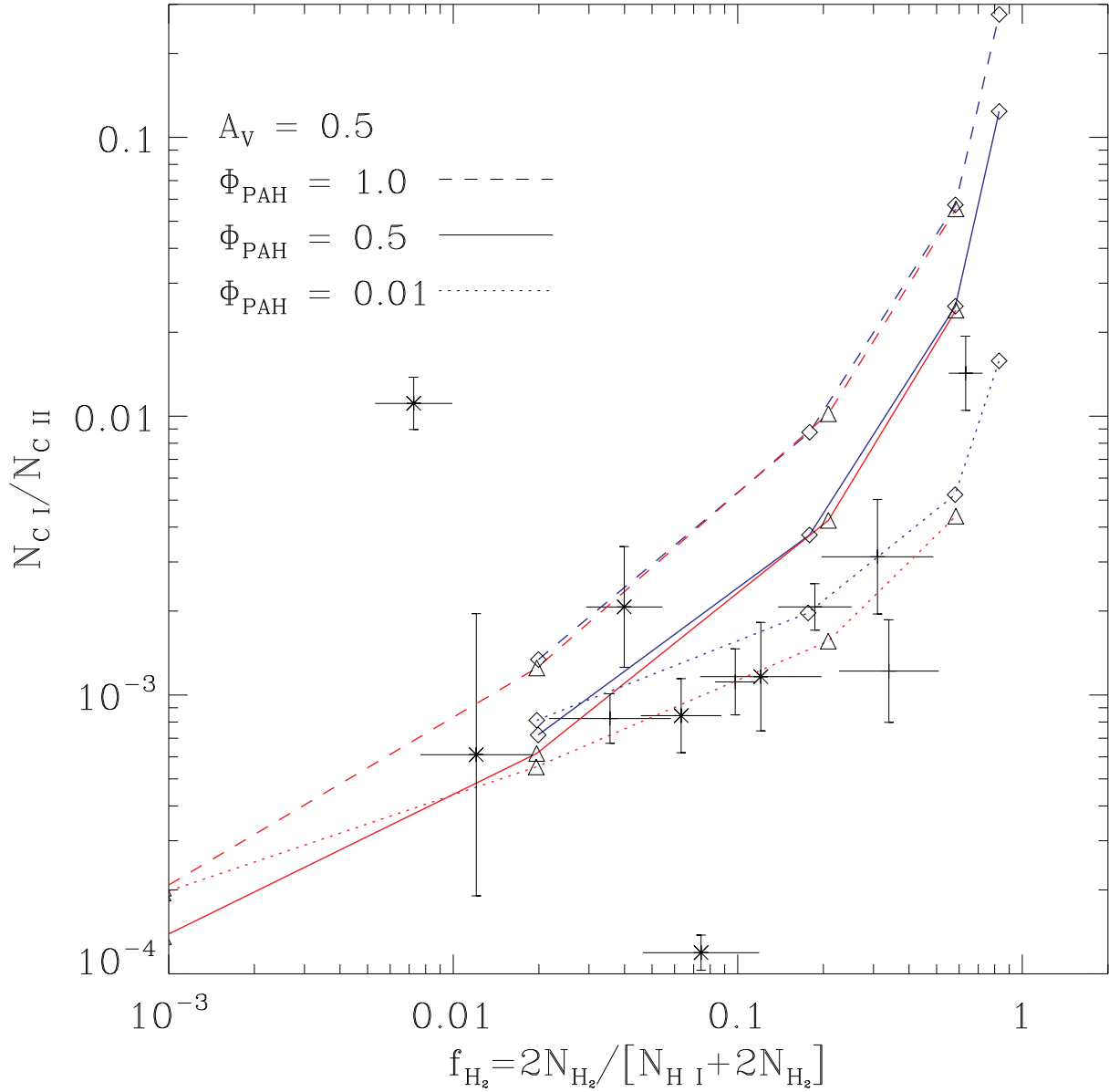


Fig. 2.— Column density ratio $N_{\text{C I}}/N_{\text{C II}}$ versus molecular hydrogen fraction $f_{\text{H}_2} = 2N_{\text{H}_2}/[N_{\text{H I}} + 2N_{\text{H}_2}]$. Observations are shown for cloud column densities in the range $0.25 \lesssim A_V \lesssim 0.75$, and $N_{\text{H}_2} > 10^{18} \text{ cm}^{-2}$. Clouds with $A_V < 0.5$ are indicated with an “×”. Curves show model results for cloud column $A_V = 0.5$, $R = 3 \times 10^{-17} \text{ cm}^3 \text{ s}^{-1}$, and $\Phi_{\text{PAH}} = 1.0$ (*dash*), $\Phi_{\text{PAH}} = 0.5$ (*solid*), and $\Phi_{\text{PAH}} = 0.01$ (*dot*). The ratio G_0/n varies along each model curve with higher G_0/n yielding smaller values of f_{H_2} . Individual models are shown with $n = 10, 30, 100$, and 300 cm^{-3} and $G_0 = 1.7$ (\diamond ; *Blue*) and $G_0 = 5.1$ (\triangle ; *Red*). For $f_{\text{H}_2} = 0.02$, $G_0/n \sim 1.7/10$ and for $f_{\text{H}_2} = 0.2$, $G_0/n \sim 1.7/30$.

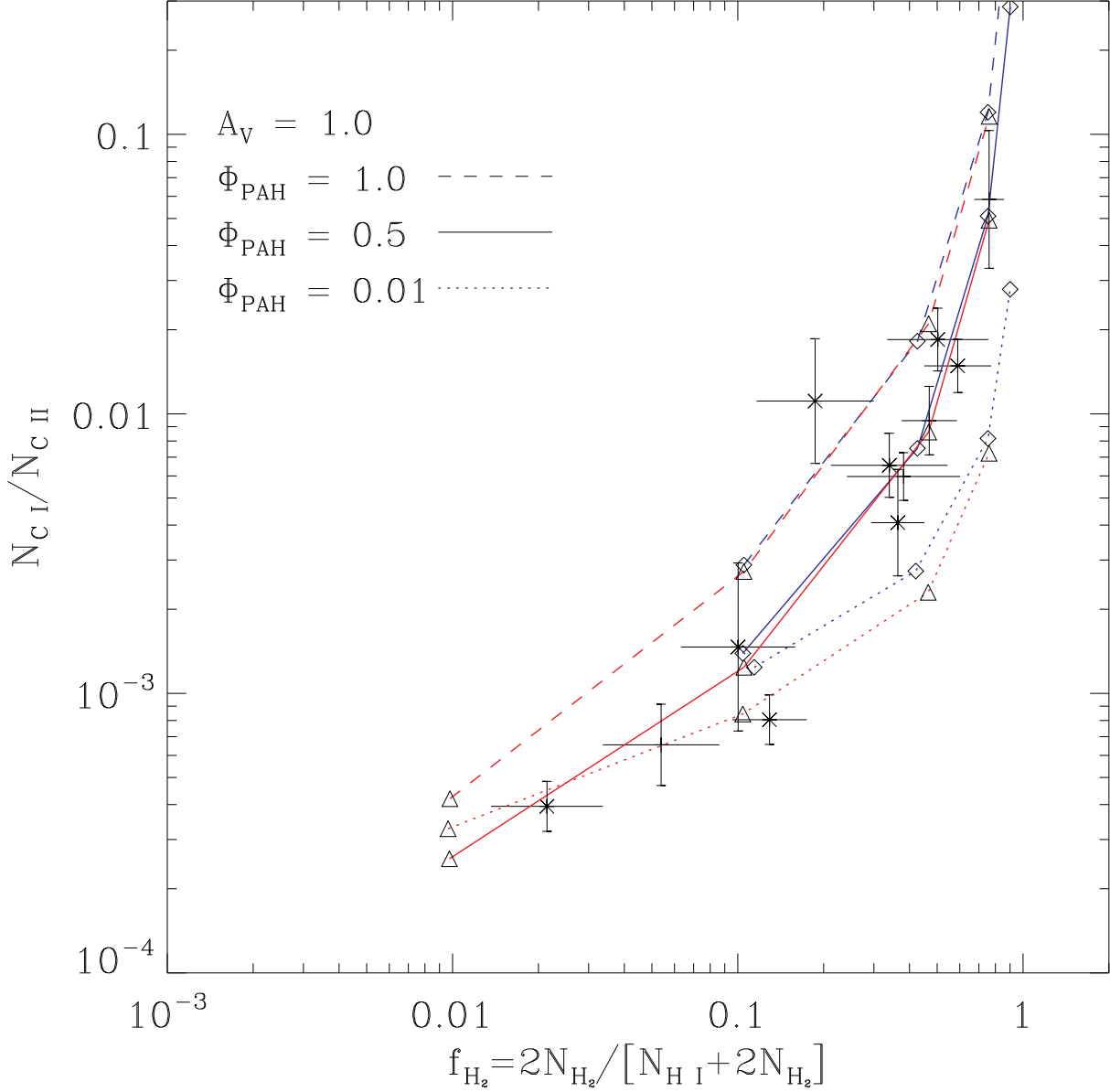


Fig. 3.— Column density ratio $N_{\text{C I}}/N_{\text{C II}}$ versus molecular hydrogen fraction $f_{\text{H}_2} = 2N_{\text{H}_2}/[N_{\text{H I}} + 2N_{\text{H}_2}]$. Observations are shown for cloud column densities in the range $0.75 \lesssim A_V \lesssim 1.25$ and $N_{\text{H}_2} > 10^{18} \text{ cm}^{-2}$. Clouds with $A_V < 1.0$ are indicated with an “×”. Curves show model results for cloud column $A_V = 1.0$, $R = 3 \times 10^{-17} \text{ cm}^3 \text{ s}^{-1}$, and $\Phi_{\text{PAH}} = 1.0$ (*dash*), $\Phi_{\text{PAH}} = 0.5$ (*solid*), and $\Phi_{\text{PAH}} = 0.01$ (*dot*). The ratio G_0/n varies along each model curve with higher G_0/n yielding smaller values of f_{H_2} . Individual models are shown with $n = 10, 30, 100$, and 300 cm^{-3} and $G_0 = 1.7$ (\diamond ; *Blue*) and $G_0 = 5.1$ (\triangle ; *Red*).

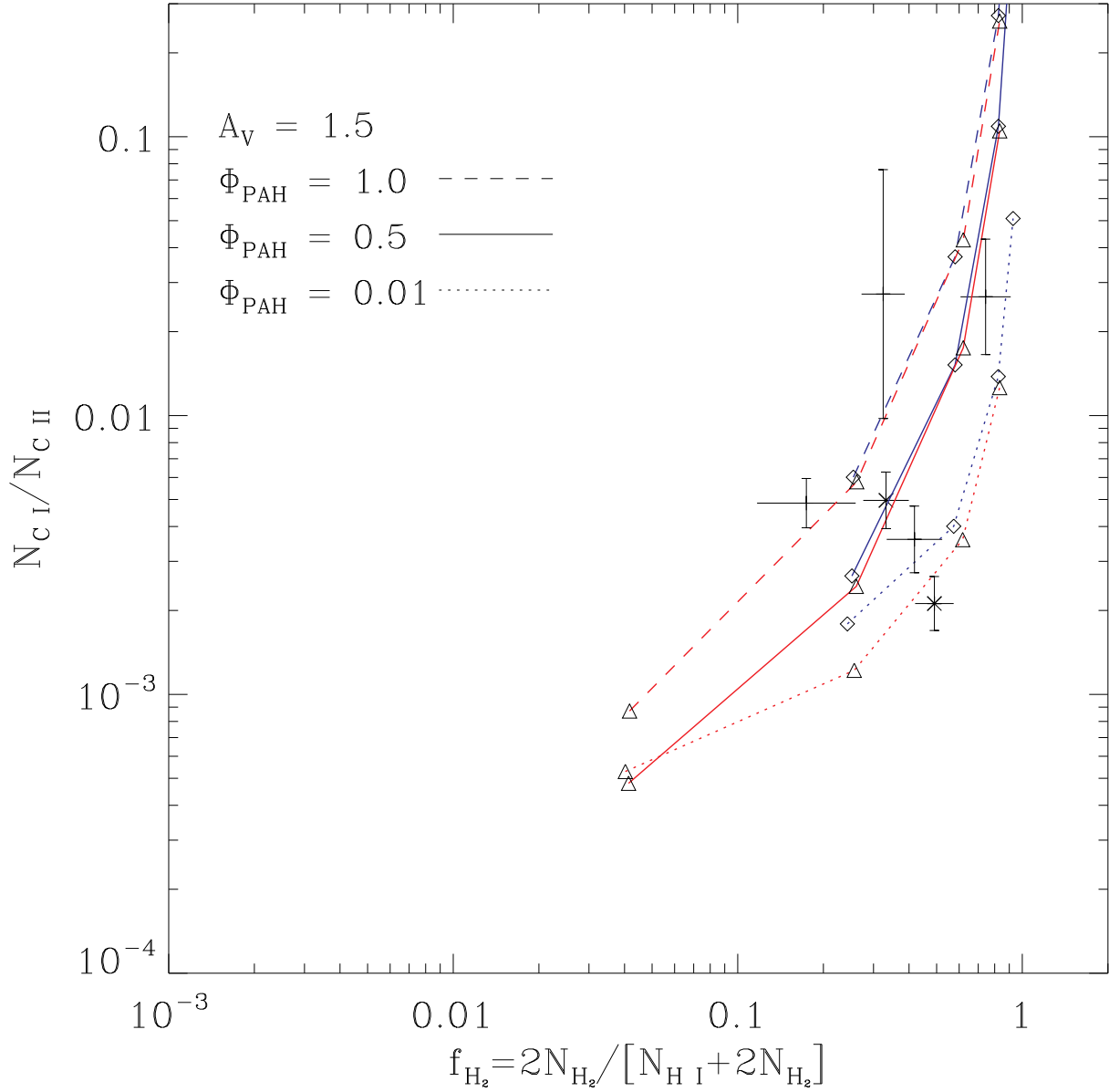


Fig. 4.— Column density ratio $N_{\text{C I}}/N_{\text{C II}}$ versus molecular hydrogen fraction $f_{\text{H}_2} = 2N_{\text{H}_2}/[N_{\text{H I}} + 2N_{\text{H}_2}]$. Observations are shown for cloud column densities in the range $1.25 \lesssim A_V \lesssim 2.13$ and $N_{\text{H}_2} > 10^{18} \text{ cm}^{-2}$. Clouds with $A_V < 1.5$ are indicated with an “×”. Curves show model results for cloud column $A_V = 1.5$, $R = 3 \times 10^{-17} \text{ cm}^3 \text{ s}^{-1}$, and $\Phi_{\text{PAH}} = 1.0$ (*dash*), $\Phi_{\text{PAH}} = 0.5$ (*solid*), and $\Phi_{\text{PAH}} = 0.01$ (*dot*). The ratio G_0/n varies along each model curve with higher G_0/n yielding smaller values of f_{H_2} . Individual models are shown with $n = 10, 30, 100,$ and 300 cm^{-3} and $G_0 = 1.7$ (\diamond ; *Blue*) and $G_0 = 5.1$ (\triangle ; *Red*).

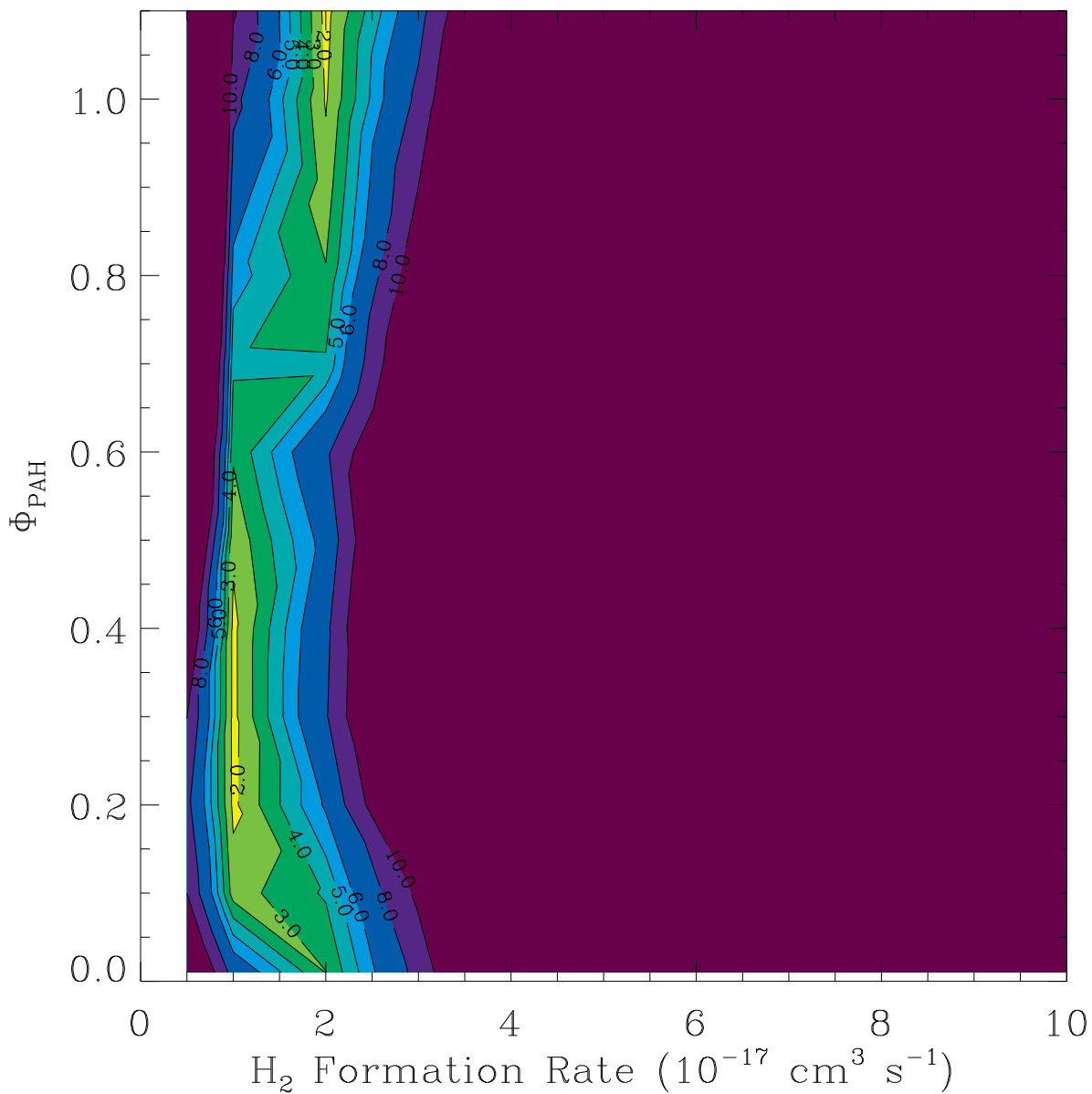


Fig. 5.— χ^2 plot of Φ_{PAH} versus H_2 formation rate R . Contour levels are $\chi^2 = 2, 3, 4, 5, 6, 8,$ and 10 . Observations are restricted to cloud column densities in the range $0.03 \lesssim A_V \lesssim 0.25$ and $N_{\text{H}_2} < 10^{17} \text{ cm}^{-2}$. The minimum value of $\chi^2_{\text{min}} = 1.6$ with 10 sources included.

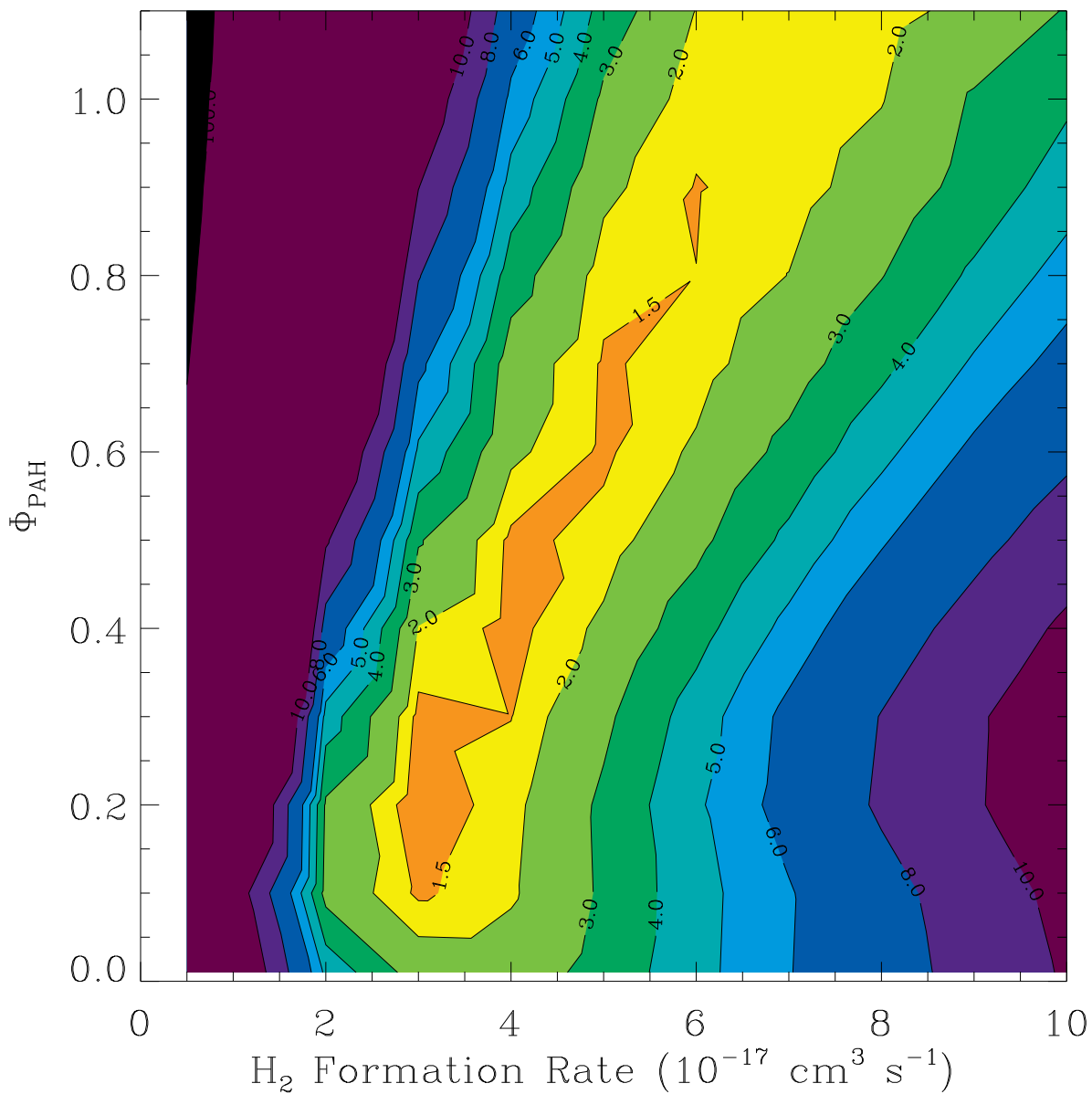


Fig. 6.— χ^2 plot of Φ_{PAH} versus H_2 formation rate R . Contour levels are $\chi^2 = 1.5, 2, 3, 4, 5, 6, 8,$ and 10 . Observations are restricted to cloud column densities in the range $0.25 \lesssim A_V \lesssim 0.75$ and $N_{\text{H}_2} > 10^{18} \text{ cm}^{-2}$.

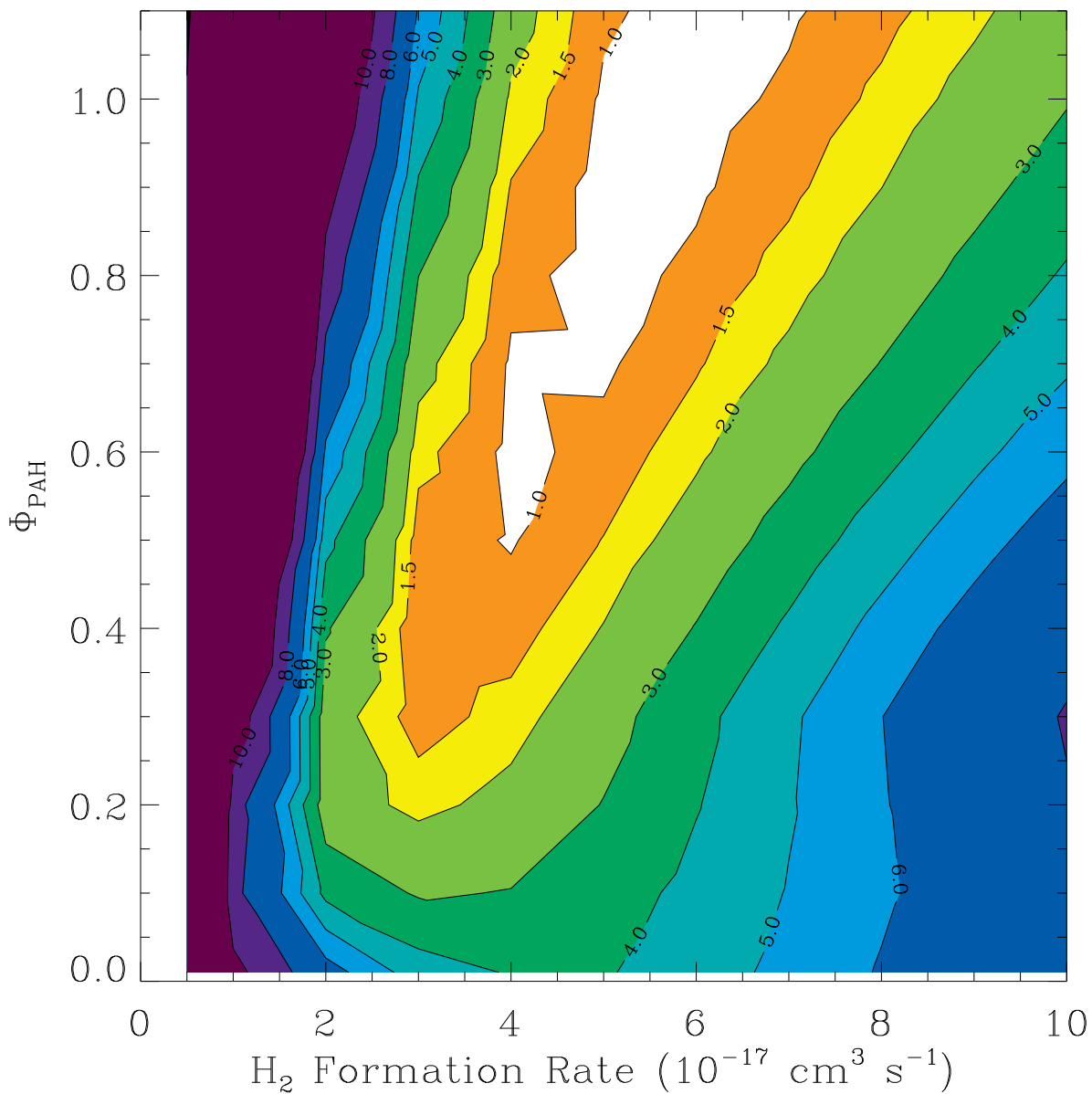


Fig. 7.— χ^2 plot of Φ_{PAH} versus H₂ formation rate R . Contour levels are $\chi^2 = 1, 1.5, 2, 3, 4, 5, 6, 8,$ and 10 . Observations are restricted to cloud column densities in the range $0.75 \lesssim A_V \lesssim 1.25$ and $N_{\text{H}_2} > 10^{18} \text{ cm}^{-2}$.

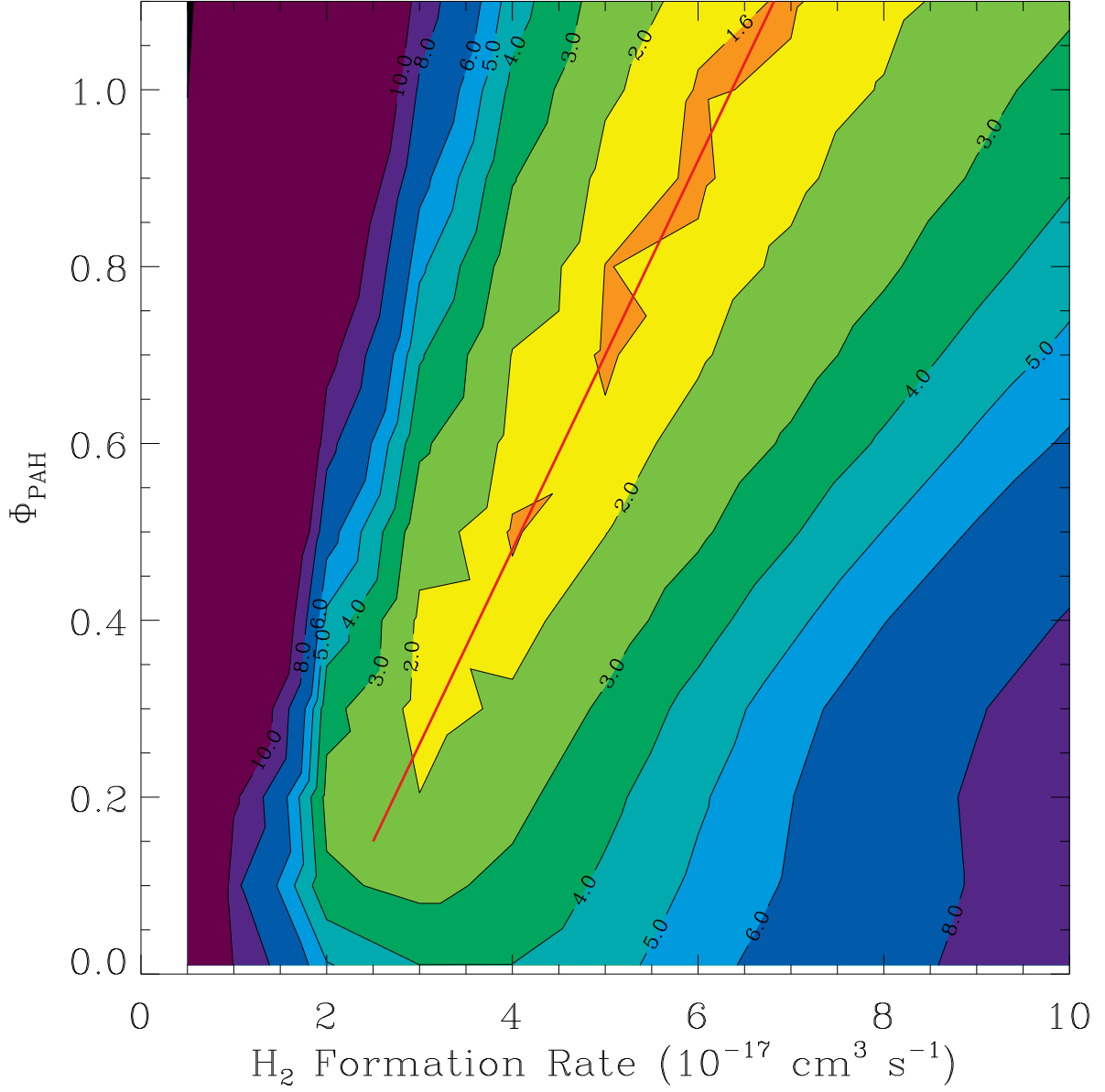


Fig. 8.— χ^2 plot of Φ_{PAH} versus H_2 formation rate R . Contour levels are $\chi^2 = 1.6, 2, 3, 4, 5, 6, 8,$ and 10 . Observations are restricted to cloud column densities in the range $0.25 \lesssim A_V \lesssim 2.13$ and $N_{\text{H}_2} > 10^{18} \text{ cm}^{-2}$. The minimum trough is given by $\Phi_{\text{PAH}} = 0.22(R/10^{-17} \text{ cm}^3 \text{ s}^{-1}) - 0.40$

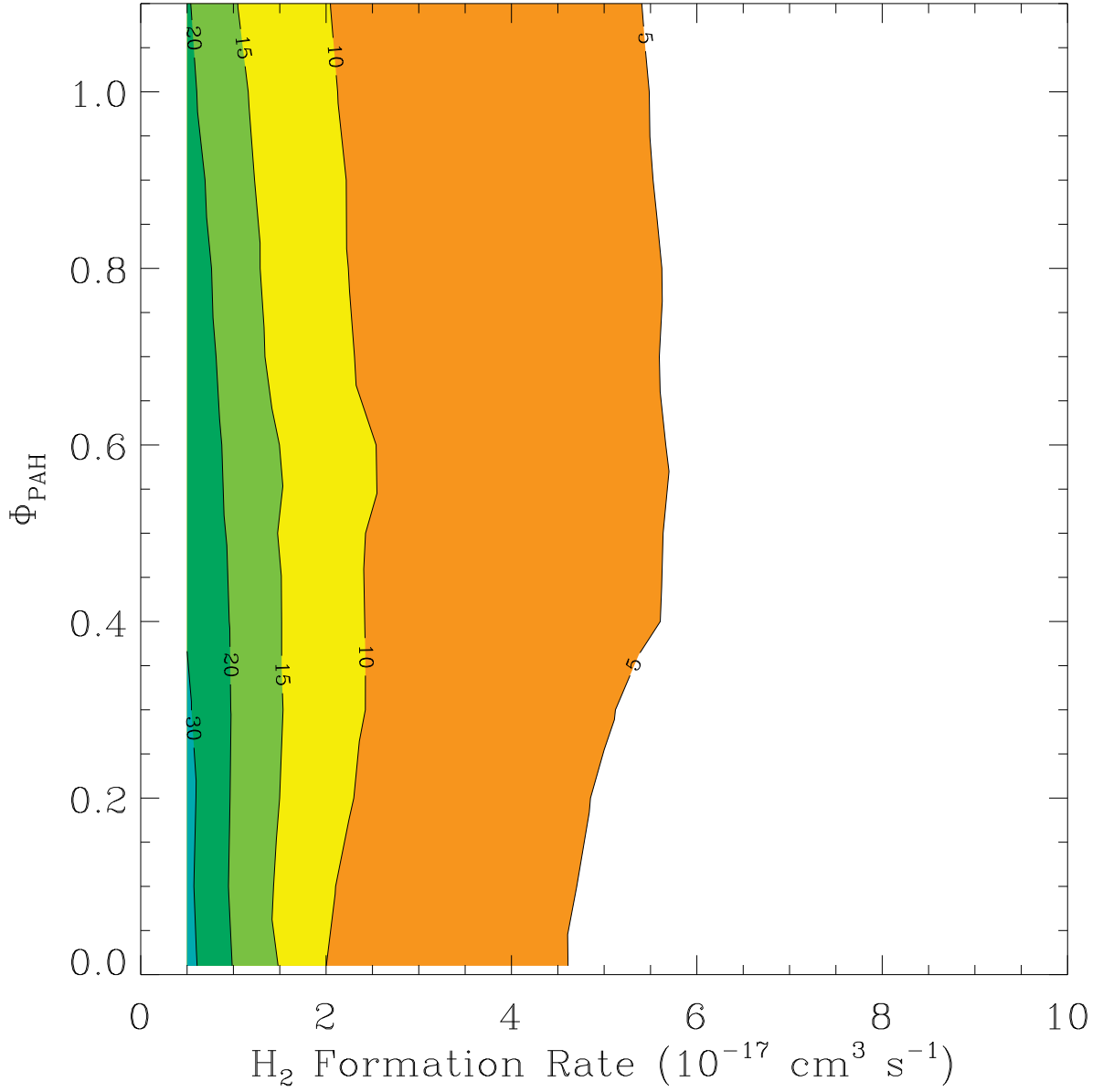


Fig. 9.— Mean density plot of Φ_{PAH} versus H_2 formation rate R . Contour levels are $\langle n \rangle = 5, 10, 15, 20,$ and 30 cm^{-3} . Observations are restricted to cloud column densities in the range $0.03 \lesssim A_V \lesssim 0.25$ and $N_{\text{H}_2} < 10^{17} \text{ cm}^{-2}$.

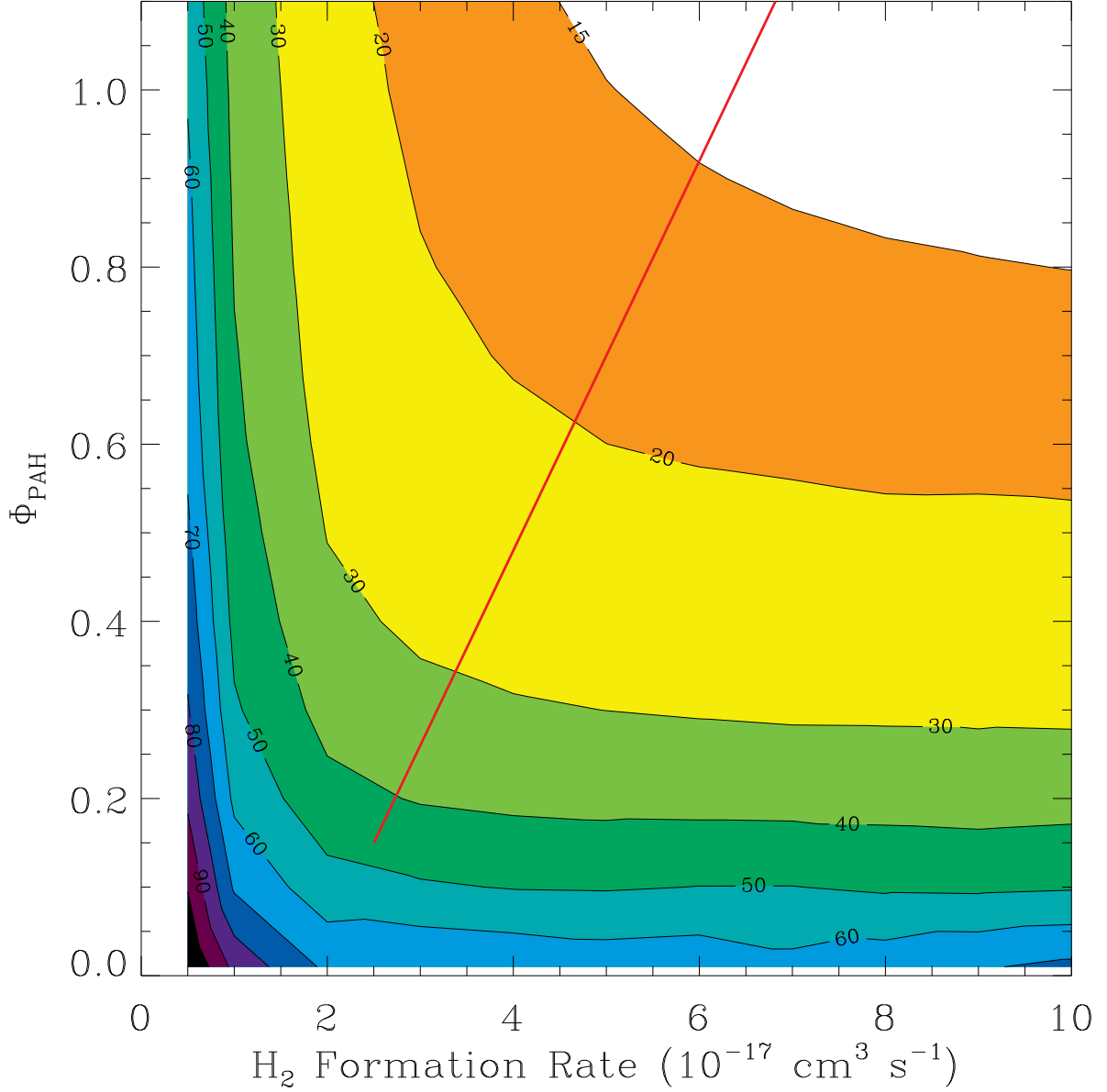


Fig. 10.— Mean density plot of Φ_{PAH} versus H_2 formation rate R . Contour levels are $\langle n \rangle = 15, 20, 30, 40, 50, 60, 70, 80, 90,$ and 100 cm^{-3} . Observations are restricted to cloud column densities in the range $0.25 \lesssim A_V \lesssim 2.13$ and $N_{\text{H}_2} > 10^{18}$. The minimum trough from Fig. (8) is given by $\Phi_{\text{PAH}} = 0.22(R/10^{-17} \text{ cm}^3 \text{ s}^{-1}) - 0.40$

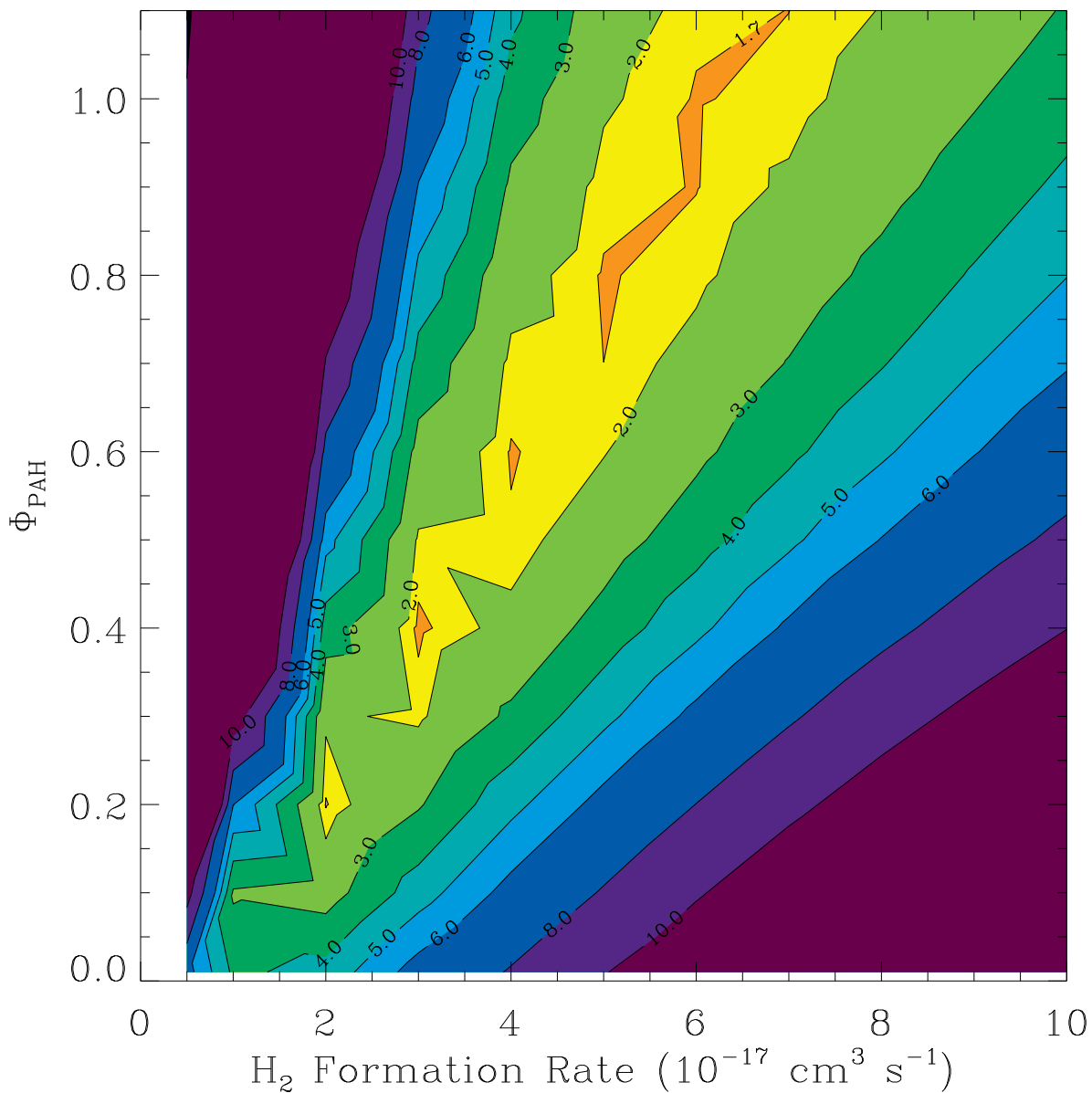


Fig. 11.— χ^2 plot of Φ_{PAH} versus H_2 formation rate R using C^+ recombination rate from Nahar & Pradhan (1997). Contour levels are $\chi^2 = 1.7, 2, 3, 4, 5, 6, 8,$ and 10 . Observations are restricted to cloud column densities in the range $0.25 \lesssim A_V \lesssim 2.13$ and $N_{\text{H}_2} > 10^{18} \text{ cm}^{-2}$.

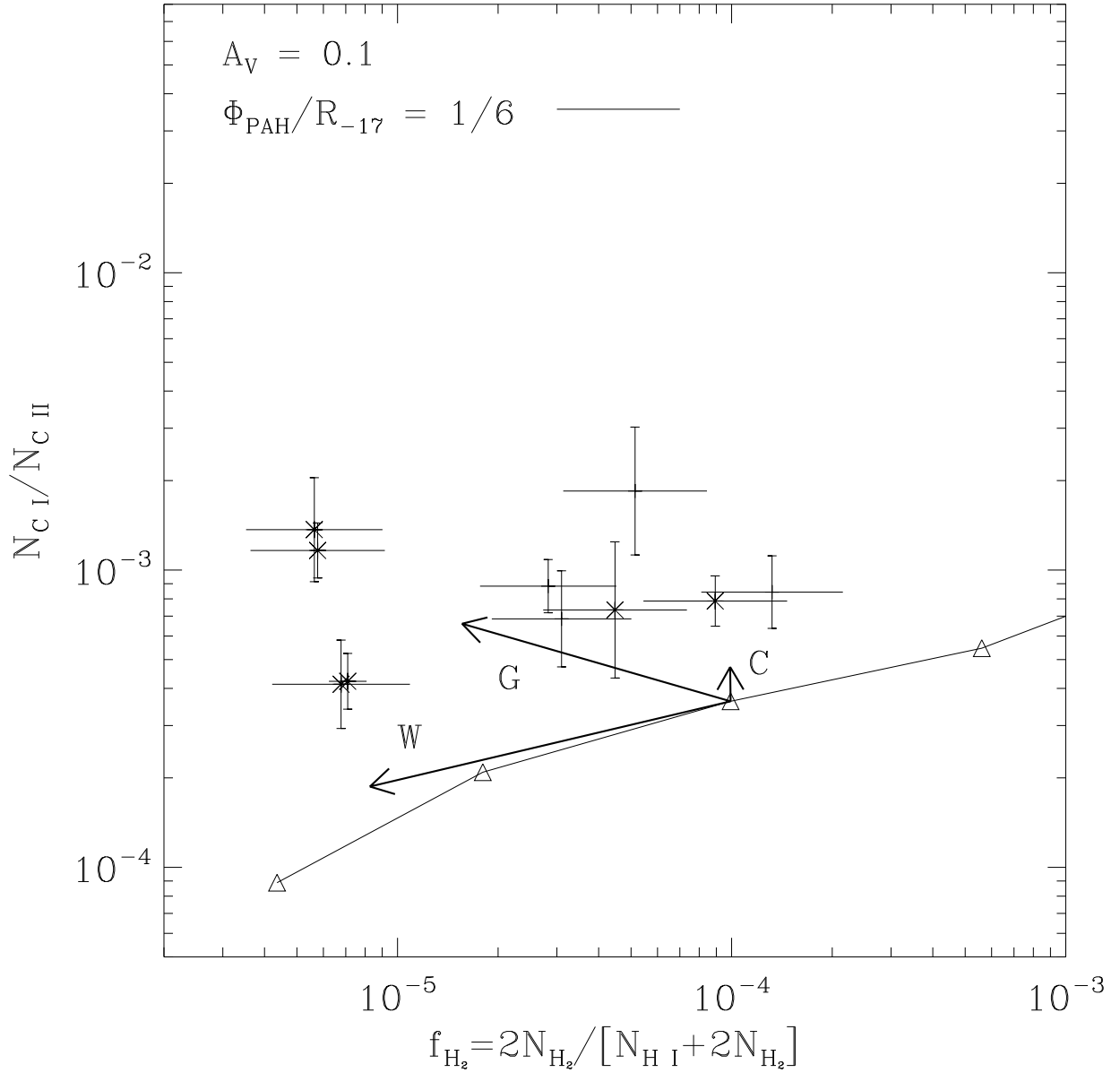


Fig. 12.— Column density ratio $N_{\text{C I}}/N_{\text{C II}}$ versus molecular hydrogen fraction $f_{\text{H}_2} = 2N_{\text{H}_2}/[N_{\text{H I}} + 2N_{\text{H}_2}]$. Observations are shown for cloud column densities in the range $0.03 \lesssim A_V \lesssim 0.25$ and $N_{\text{H}_2} < 10^{17} \text{ cm}^{-2}$. Clouds with $A_V < 0.1$ are indicated with an “x”. Curves show model results for cloud column $A_V = 0.1$, and $\Phi_{\text{PAH}} = 0.5$, $R = 3 \times 10^{-17} \text{ cm}^3 \text{ s}^{-1}$ ($\Phi_{\text{PAH}}/R = 1/6$; *solid*). The ratio G_0/n varies along each model curve with higher G_0/n yielding smaller values of f_{H_2} . Individual models are shown with $n = 10, 20, 30,$ and 40 cm^{-3} and $G_0 = 5.1$ (Δ). Arrows show the affects of lines of sight which graze a larger ($A_V = 1$) cloud ('G'), have cosmic rays enhanced by a factor of 10 ('C'), and have half the column density in the WNM phase ('W').